Effects of Large Scale Interfacial Roughness on Giant Magnetoresistance in Exchange Biased Spin Valves and Co/Cu Multilayers

A thesis submitted in partial fulfillment of the requirements

for the degree Bachelors of Science with Honors in

Physics from the college of William and Mary in Virginia,

by

Dimitar M. Vlassarev

Accepted for Honors

_____

Advisor: Prof. Anne Reilly

_____

Prof. Christopher Carone

_____

Prof. William Cooke

_____

Prof. Brian Holloway

Williamsburg, Virginia

April 2005

Contents

List of Figures **3**

Abstract **5**

1. Introduction **6**

2. Theory **7**

2.1 Ferromagnetism 7

2.2 Anti-Ferromagnetism and Exchange Biasing 11

2.3 Giant Magnetoresistance 14

2.4 Magnetic Couplings in Thin Film Multilayers 21

2.5 Anisotropic Magnetoresistance 24

2.6 Effects of Roughness 25

3. Experiment **27**

3.1 Rough Substrates 27

3.2 Giant Magnetoresistive Multilayers 28

3.3 Giant Magnetoresistive Measurements. 29

3.4 Roughness Measurements 35

3.5 A Note on Error Bars 36

4. Results **36**

4.1 Co/Cu Multilayer Data and Analysis 36

4.3 EBSV Data 42

4.3.1 EBSV Roughness Data 42

4.3.2 Resistivity Calculations and Magnetic Properties of EBSV Samples 48

4.3.3 Electric Properties of EBSV Samples 53

4.4 EBSV Data Analysis 54

5. Conclusions and Future Work **63**

Bibliography **65**

Acknowledgments **67**

Appendix I – LabView Virtual Instruments' Snapshots **68**

List of Figures

1. Domains in ferromagnetic materials. 9
2. Domain realignment under external magnetic fields 10
3. Hysteresis loop explained. 10
4. Magnetic moments in anti-ferromagnetic materials. 11
5. Representation of a pinned Co layer adjacent to FeMn. 12
6. A hysteresis loop for an exchange biased sample. 13
7. Effects of spin dependent scattering in multilayers. 15
8. GMR loop. 16
9. Channeling in GMR multilayers. 17
10. Schematic depiction of the available electronic states in a Co/Cu/Co stack. . . 18
11. Approximate semi-classical solution for the current density of an idealized Co/Cu/Co spin valve. 20
12. Schematic representation of orange peel coupling. 22
13. Polymer spheres on silicon substrate and evaporated metal nanodot pattern. . 27
14. Magnetic field calibration. 30
15. Coercivities, exchange bias, coupling field and resistivity in a GMR curve. . . 34
16. Schematic depicting of the operating principle of an atomic force microscope. 35
17. Co/Cu 50nm nanosphere, AFM scan. 38
18. Resistance perpendicular to field in Co/Cu bare multilayer. 39
19. Resistance parallel to field in Co/Cu bare multilayer. 40
20. Resistivity in Co/Cu bare multilayer. 41
21. 3D image of EBSV on 320nm nanosphere sample. 43

22. Sectional AFM scan of EBSV on 320nm nanosphere sample. 44

23. 3D image of EBSV on 560nm nanosphere sample. 45

24. Sectional AFM scan of EBSV on 560nm nanosphere sample. 46

25. Resistance perpendicular to field in a bare EBSV sample. 49

26. Resistance parallel to field in a bare EBSV sample. 50

27. Resistivity in a bare EBSV. 51

28. A plot of the GMR% vs. minimum resistivity in EBSV samples. 54

29. Maximum resistivity vs. minimum resistivity in EBSV samples. 55

30. Minimum resistivity and GMR% vs roughness in EBSV samples. 57

31. Orange peel modeling magnetic coupling in EBSV samples. 59

32. Coupling field in the EBSV samples versus RMS roughness. 61

33. Orange peel fit to the coupling field with an offset. 62

Abstract

This thesis explores the relationship between substrate roughness and the giant magnetoresistive properties of exchange biased spin valves and Co/Cu multilayers. For this purpose controlled roughness is introduced onto Si substrates and the appropriate thin film structure is sputtered. Giant magnetoresistance is measured and correlated with atomic force microscopy roughness measurements. Substrate roughness leads to interfacial roughness which is related to giant magnetoresistance through its effects on electron scattering and magnetic ordering through oscillatory interlayer exchange, "orange peel" and pinhole couplings. Results suggest that the dominant effect on giant magnetoresistance is a decrease due to increasing total film resistivity with higher roughness. While an increase in magnetic coupling was also observed it seemed to have no significant effect on giant magnetoresistance in exchange biased spin valves.

1 Introduction

"Spintronics" has the potential to revolutionize electronics. The basic idea behind spintronics is to use the spin of the electron in addition to its charge to regulate currents. One spin-based effect seen in magnetic thin film multilayers is giant magnetoresistance (GMR). GMR is a relatively large change in resistance experienced by a multilayer under the influence of an applied magnetic field. This phenomenon has many important practical applications.

Sensors based on GMR have allowed an unprecedented increase in hard disk drive capacity [1]. Significantly better sensitivity of GMR sensors, compared to inductive sensors, allows for much higher data densities. Another important application is Magnetic Random Access Memory (MRAM). Such devices may end up revolutionizing nonvolatile flash storage [2]. Radiation-hardened MRAM also has potential applications in military and aerospace systems [3].

This thesis explores the effects of interfacial roughness on current in plane GMR. Past studies of roughness effects have focused on small-scale interfacial roughness introduced by growth conditions, such as vacuum chamber pressure. There is very little work done exploring the effect of large scale substrate roughness on interfacial roughness and GMR. It is important to be able to predict the behavior of GMR structures on novel substrates with inherent roughness. This will allow for GMR multilayers to be deposited on a wide variety of materials other than the common silicon wafer. While the main focus of the project is an exchange biased spin valve, effects of substrate roughness on Co/Cu mutilayers are also considered.

Various magnetic couplings are responsible for GMR in both structures. It is important to consider the effects of interfacial roughness on these couplings in order to understand how GMR will be affected. There are also other more subtle consequences of interfacial roughness on GMR that must be considered. It is important to understand the individual contributions of these effects on GMR in order to obtain a better comprehension of the effects of large scale interfacial roughness on GMR.

2 Theory

2.1 Ferromagnetism

Ferromagnetic materials are the basis of GMR. In exchange biased spin valves it is also important to understand the anti-ferromagnetic properties of materials such as FeMn. Generally, magnetization in ferromagnetic solids results from the spin orientation of the electrons in the material. Angular momentum has a much smaller contribution [11].

Ferromagnetism is a purely quantum mechanical effect resulting from electron-electron interactions. The total wave function of two electrons in the electron cloud has to be anti-symmetric due to the Pauli exclusion principle. For a spin triplet state the spatial wave function will be anti-symmetric providing separation between the electrons and minimizing the Coulomb repulsion. On the other hand, a spin singlet state will have a higher energy due to a stronger Coulomb interaction.

A simple representation of the interaction energy has the following form,

$$E_{\text{int}} = -\alpha \overrightarrow{S_1} \cdot \overrightarrow{S_2} \tag{1}$$

where α can be calculated from the Coulomb term in the Hamiltonian and $\overrightarrow{S_1}$ and $\overrightarrow{S_2}$ are the spins of the two electrons. Note that in ferromagnetic materials α is positive. Rewriting equation (1) in combined spin basis,

$$E_{\text{int}} = -\alpha(\frac{\vec{S}^2}{2} + \frac{3}{4}\hbar^2) \tag{2}$$

where $\vec{S}$ is the total spin of the two electrons. It is clear from equation (2) that it would be energetically beneficial for the electrons to maximize their total spin by aligning themselves in the same direction.

Thermal energy of the electrons counteracts to an extent this tendency of spin alignments. Above a critical temperature the long term order established by the interaction in (2) is lost. This temperature is referred to as the Curie temperature and for Co it is 1404K [12]. It is clear that at room temperature we can expect Co electrons to align.

Aligning all electron spins in the same direction does not provide the lowest energy configuration in the absence of an external field. Domains, which are sections of the ferromagnetic material with homogeneous magnetization, form to minimize the total energy. If we had a single domain magnetostatic energy due to the resulting field would offset the benefits of minimizing exchange energy. Magnetostatic energy thus favors the

presence of more domains that tend to cancel out their magnetic fields. Crystalline structure also dictates that magnetizing a sample along different direction requires different external fields. This leads to a preference in the magnetization direction of the domains. Mangetostrictive energy is the result of changes in the dimensions of the sample depending on the magnetization. Balancing all the energies mentioned above produces a complex domain pattern with average domain size of about 10μm [13].

An external field simplifies the situation a bit. Domains that are aligned with the external field tend to grow at the expense of other domains and eventually the material obtains a homogeneous magnetization in the same direction as the external field [13]. Figures 1 and 2 illustrate this process.

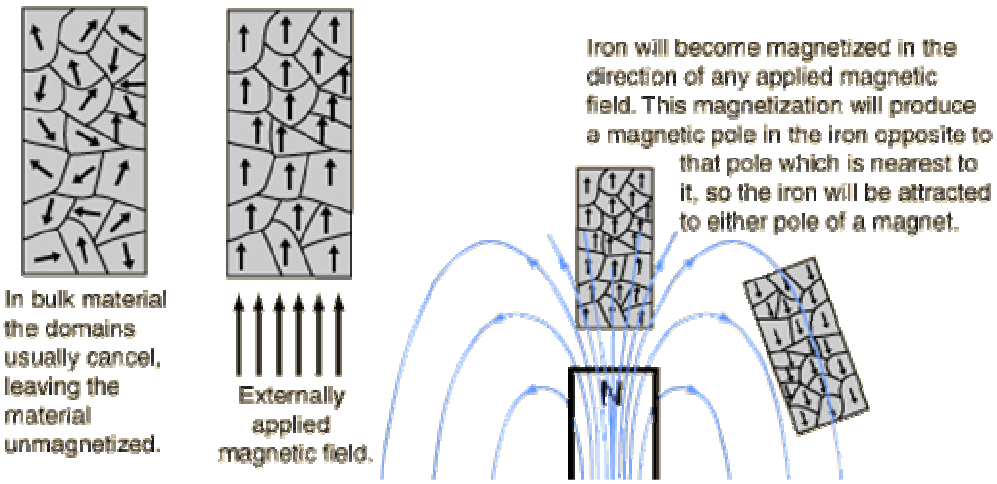

Figure 1. Domains tend to align with external fields in order to minimize the energy of the system.

(picture obtained from http://hyperphysics.phy-astr.gsu.edu/hbase/solids/ferro.html)

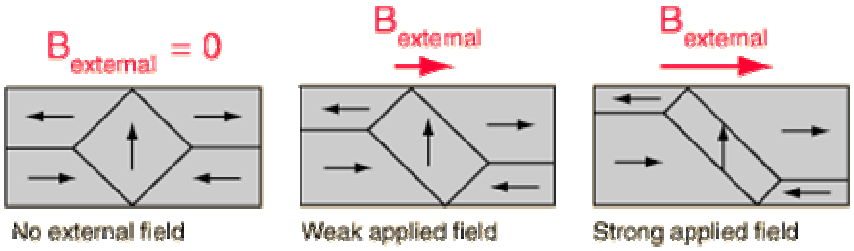

Figure 2. Domains that are closely aligned with the external field grow at the expense of other domains.

(picture obtained from http://hyperphysics.phy-astr.gsu.edu/hbase/solids/ferro.html)

After the external field is turned off many of the domains retain their current orientation. This results in a hysteresis loop when the magnetization is plotted against the applied external field [13]. The resulting curve is shown in Figure 3. One important property of the magnetic material can be obtained by finding x-intercepts of the graph in Figure 3. The average of the absolute values of the intercepts is the coercivity H_C and it determines how easy or difficult it is to demagnetize a sample.

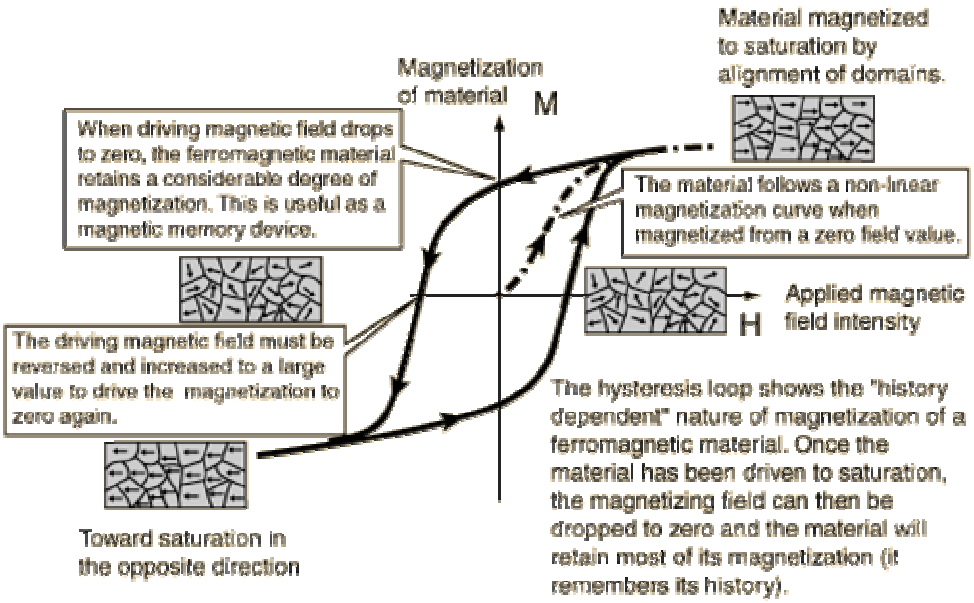

Figure 3. Hysteresis loop in a ferromagnetic material.

(picture obtained from http://hyperphysics.phy-astr.gsu.edu/hbase/solids/hyst.html)

2.2 Anti-Ferromagnetism and Exchange Biasing

Some GMR multilayers use anti-ferromagnetic materials. In anti-ferromagnetic materials α as introduced in equation (2) is negative resulting in a preference for the spin singlet electronic state. Just like ferromagnetic materials there exists a critical temperature beyond which this order is lost. This temperature is called the Neel temperature and for FeMn it is about 500K [14]. The Fermi structure dictates the anti-ferromagnetic arrangement schematically shown in Figure 4 [13].

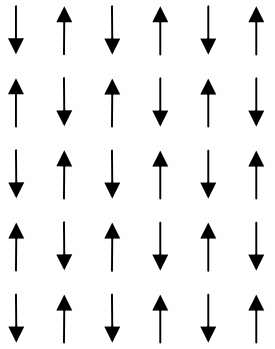

Figure 4. Schematic representation of magnetic moment distribution in an anti-ferromagnetic material.

Anti-ferromagnetic (AFM) materials such as FeMn can be used to "pin" adjacent ferromagnetic (FM) layers such as Co in GMR multilayers. Pinning is caused by the exchange bias interactions across the AFM/FM interface. This is achieved by heating the multilayer close to the Neel temperature of the anti-ferromangetic material but well bellow the Curie temperature of the ferromagnetic layer and then cooling down the structure in a uniform magnetic field. The FM layer will align itself with the external field. This will align the AFM layer magnetic moments, at the AFM/FM interface, with

the applied field. Since this happens near the Neel temperature, the remaining magnetic moments in the AFM layer will order themselves accordingly [13]. In the end the structure depicted in Figure 5 is achieved.

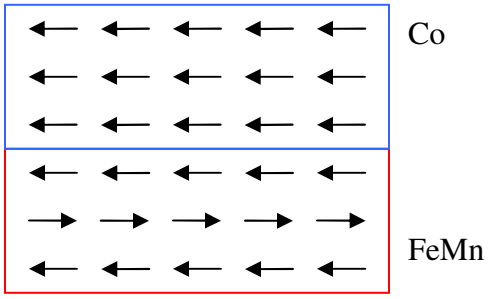

Figure 5. Pinned Co layer in a thin film multilayer.

Breaking the anti-ferromagnetic ordering in FeMn requires a significant amount of energy and is not achieved even when the Co layer is magnetized opposite to the interface magnetization of the FeMn. The Co layer in Figure 5 is under the influence of the FeMn magnetization at the interface which means that it would be difficult to magnetize the Co layer to the right, and its magnetization is in a sense “pinned”. This leads to a shift in the hysteresis loop, which is defined by the exchange bias field H_{EB} (see Figure 6) [13]. The FrMn/Co structure is highly anisotropic and extremely useful in producing GMR.

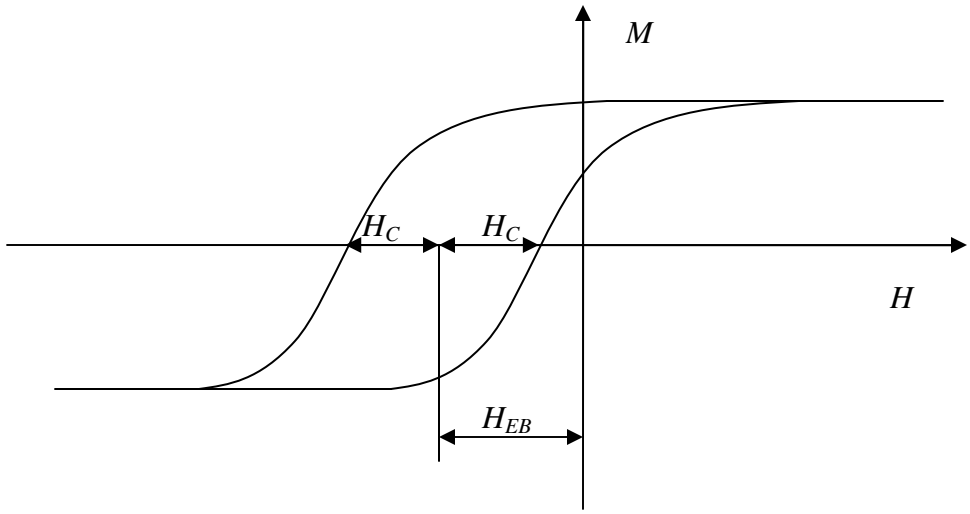

Figure 6. A hysteresis loop for an exchange biased sample. Coercivity and exchange biased fields are shown.

2.3 Giant Magnetoresistance

Giant magnetoresistance was first observed in 1988 in Fe/Cr layered structures [4,5] and has since been seen in a large variety of thin film multilayers. GMR is defined as a large change in resistance measured in an applied magnetic field. The external field orientates the magnetizations of the ferromagnetic layers in the multilayers to achieve parallel and anti-parallel alignment, as shown in Figure 7. The basic process giving rise to GMR is spin-dependent electron scattering. Current flows through a ferromagnetic (F) layer with certain magnetization, and depending on the magnetization of the next ferromagnetic layer, different degrees of electron scattering will occur [6]. See Figure 8 for a sample GMR curve and the magnetization alignments in the different states.

The Camley Barnas theory (CB), which is outlined below, describes the basic behavior. Let's consider the simplified multilayer structure of a ferromagnetic material, conducting (C) spacer layer and another ferromagnetic material. We consider two cases of alignment of the magnetic moments of the ferromagnetic layers: parallel and anti-parallel. Assuming all electrons with spin opposite to that of the next layer scatter at the interfaces we get the following estimate. Electrons with spin that is aligned with the ferromagnetic moment have a mean free path of roughly $3t$ (no scattering), where t is the thickness of each layer. On the other hand, electrons that are anti-aligned with the magnetic moment of the ferromagnetic layers have a mean free path of t (scatter at both interfaces). This gives us an average mean free path of $2t$ when the two ferromagnetic

layers are aligned. In the case of the two ferromagnetic layers having opposite magnetic moments, electrons aligned with either ferromagnetic layer scatter once resulting in a mean free path of 1.5*t*. The decrease in mean free path results in an increase in resistivity for the anti-parallel alignment. This model assumes that the mean free path of the electron λ in either the spacer or the ferromagnetic material is larger then *t* which is indeed the case in the structures considered here.

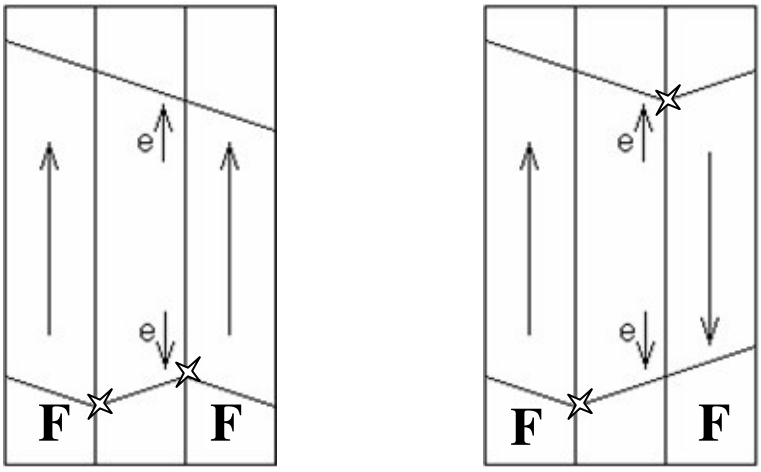

Figure 7. When the two ferromagnetic layers are aligned spin up electrons have mean free path of 3*t* and spin down 1*t*. This gives us average mean free path of 2*t*. When the two ferromagnetic layers have opposite alignment both spin up and spin down electrons have mean free paths of 1.5*t* and the average mean free path goes down to *1.5t*.

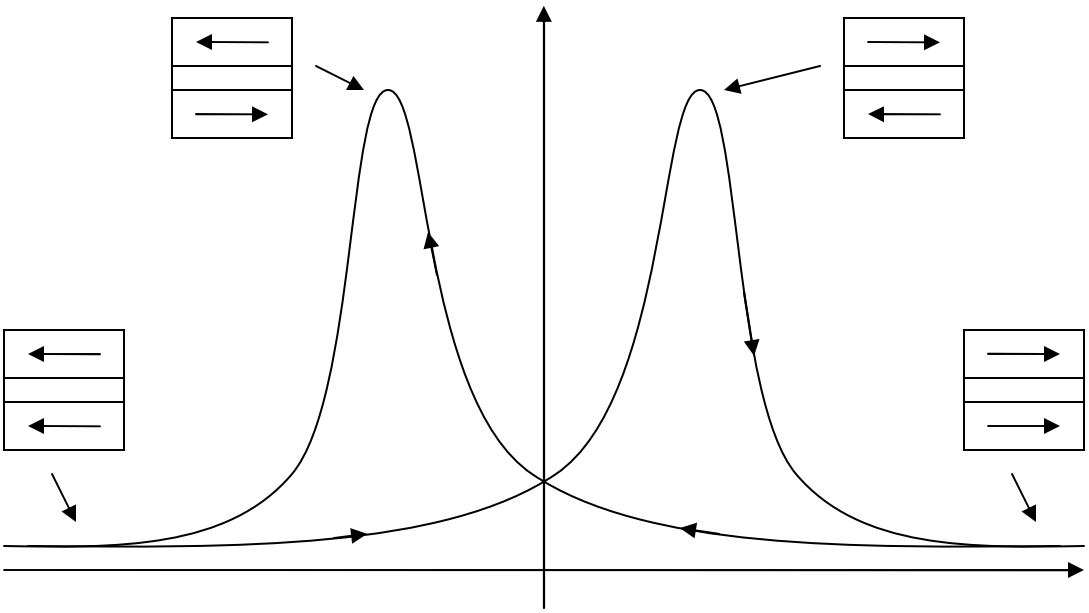

Figure 8. GMR loop. Plotted is resistivity versus applied field. Depicted are also the schematic alignments of the ferromagnetic layers.

Hood and Falicov describe a different mechanism that enhances the GMR effect [7]. Consider the case for both ferromagnetic layers aligned with the spin of an electron in the spacer layer. This electron will be "channeled" through a series of specular reflections at the interfaces between the spacer layer and the ferromagnetic layers because the spin bands in the ferromagnetic layers are filled. If the electron spin is anti-aligned with the magnetic moment of the ferromagnetic layer then it may enter into the more resistive ferromagnetic material. In the case of the two ferromagnetic materials having opposing magnetic moments (anti-parallel alignment), little or no "channeling" will occur (see Figure 9). Thus if the interfaces are smooth and the spacer material has significantly better conductance then the ferromagnetic material, "channeling" can play an important role.

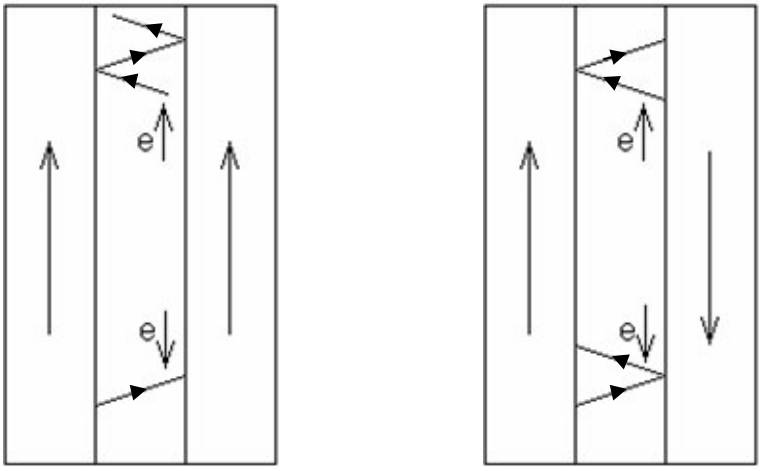

Figure 9. Spin up electrons in the spacer layer will travel their normal mean free path as they would be unable to enter the already filled spin band in the ferromagnetic material (left). This is not the case for the anti-parallel alignment of the ferromagnetic layers (right) where neither spin up nor spin down electrons, on average, experience specluar reflection more then once.

Let us examine the band structure of Co in order to better understand the scattering, reflection and transmissions at the interfaces. The density of electron states in Co that have spins aligned with an external magnetic field is much higher. As the energy of the states that are anti-aligned with the applied field increases some of these states end up well above the Fermi energy and are thus practically inaccessible. Thus an incident electron that has a spin that is anti-aligned with the magnetization of the ferromagnetic layer it is trying to penetrate is likely to scatter or reflect depending on the exact incidence angle and energy. Figure 10 shows schematically how this happens.

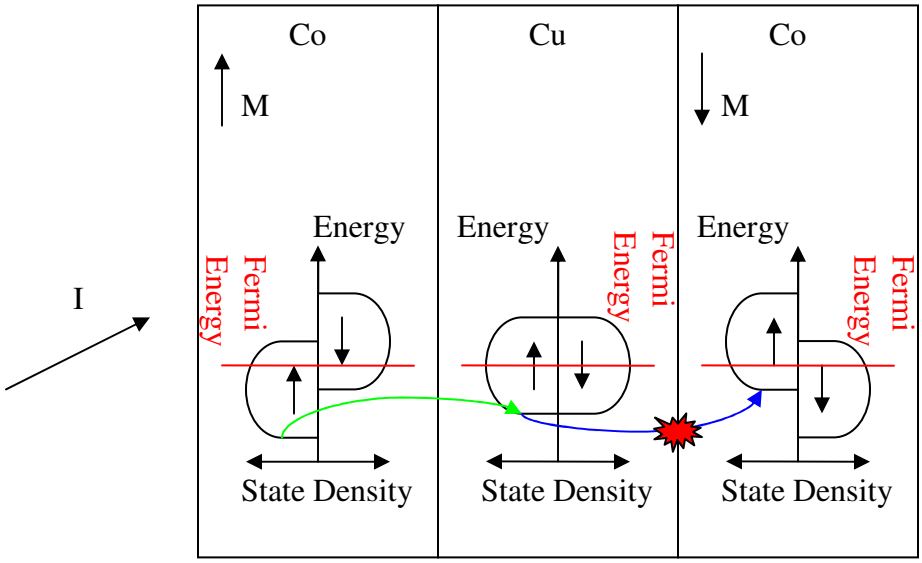

Figure 10. Schematic depiction of the available electronic states in a Co/Cu/Co stack. Note that there are very few available spin up electronic states available in the rightmost layer and scattering or reflection of spin up electrons at the interface is likely.

A complete theory of GMR involves solving the Boltzmann transport equation. An exact analytical solution for the current in plane geometry is unavailable. Current densities for an idealized Co/Cu/Co spin valve are shown in Figure 11. These are obtained from [15] and are based on a bulk resistivity of $3\mu\Omega cm$ for copper and $15\mu\Omega cm$ for Co. Among other things, these values suggest that channeling may indeed play an important role in GMR for near perfect interfaces. Unfortunately this solutions is not very helpful in realistic spin-valves especially when we factor in the roughness. Still it provides a good idea of what the current flow roughly is.

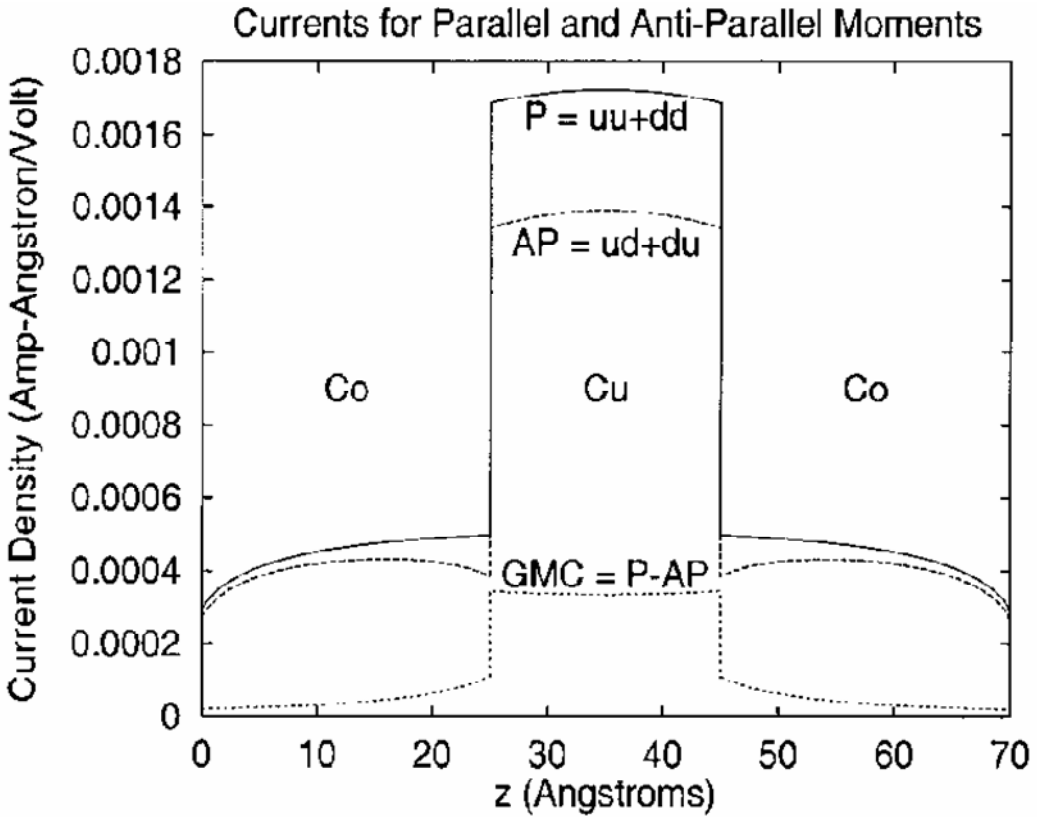

Figure 11. Approximate semi-classical solution for the current density of an idealized Co/Cu/Co spin valve. P is the conductivity for the parallel alignment and AP for the anti-parallel. GMC is the difference responsible for GMR. uu and dd are up and down spin channel conductivity respectively and ud and du are the conductivities for the AP alignment of the spin up and spin down channels [15].

2.4 Magnetic Couplings in Thin Film Multilayers

Maximum GMR effect is achieved when the magnetizations of the ferromagnetic layers can be aligned in true parallel and anti-parallel configurations. Magnetic coupling between the ferromagnetic layers thus plays a critical role in GMR. Orange peel coupling represents an interaction between magnetic poles forming on rough interfaces. Neel's model first described this form of coupling [9]. The interlayer coupling energy J is given by,

$$J_{op} = \frac{\pi^2 h^2 \mu_0 M_f M_p}{\sqrt{2}\lambda} e^{-\frac{2\pi\sqrt{2}t_{Cu}}{\lambda}} \tag{3}$$

where h is the peak-peak amplitude of the roughness and λ is the wavelength, M_f and M_p are the saturation magnetizations of the free and pinned layers respectively and t_{Cu} is the thickness of the Cu spacer layer between the two Co layers experiencing coupling. This results in a coupling field of:

$$H_{op} = \frac{J_{op}}{\mu_0 t_f M_f} = \frac{\pi^2 h^2 M_p}{\sqrt{2} t_f \lambda} e^{-\frac{2\pi\sqrt{2}t_{Cu}}{\lambda}} \tag{4}$$

where t_f is the thickness of the free layer [9]. It is important to notice that equation (4) tells us that the coupling can be either increasing or decreasing with λ. Figure 12 shows schematically the interaction responsible for orange peel coupling.

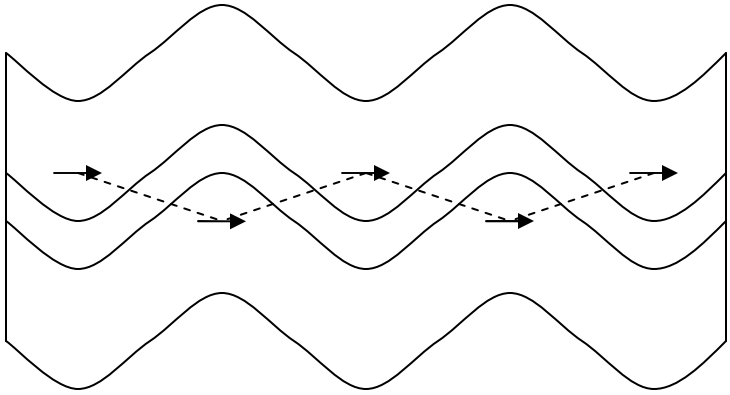

Figure 12. Schematic representation of orange peel coupling. Magnetic poles form and couple with poles in the adjacent ferromagnetic layer through the resulting magnetic fields. A thin spacer layer is also depicted.

The largest contribution to the oscillatory interlayer exchange coupling comes from RKKY coupling, named after Ruderman, Kittel, Kasuya and Yosida [8]. Oscillatory interlayer exchange coupling is responsible for the anti-ferromagnetic coupling which leads to GMR in Co/Cu superlattice multilayers. In RKKY coupling, spins in one ferromagnetic layer couple by a local exchange interaction to a conduction electron in the spacer layer which then transfers to a distant spin in another layer via another local exchange interaction. The interaction energy is

$$J_{ex} = \frac{\mu_0 E_0}{(k_0 t_{Cu})^2} \sin\left(\frac{2\pi t_{Cu}}{\Lambda} + \psi\right) \frac{T/T_0}{\sinh(T/T_0)} \qquad (5)$$

where E_0 is coupling energy, k_0 is wave number Λ is the wavelength of the coupling repeating pattern, ψ is a phase factor, T is the temperature and T_0 is a characteristic temperature [8]. The form of T_0 is,

$$T_0 = \frac{\hbar v_F}{2\pi k_B t_{Cu}} \tag{6}$$

where v_F is the Fermi velocity of the relevant electrons in the Cu layer [8]. Consider the temperature dependant term in (5) with (6) in mind,

$$\lim_{t_{Cu}\to 0} \frac{\partial}{\partial T} \frac{T/T_0}{\sinh(T/T_0)} = 0 \tag{7}.$$

So for very thin Cu layers the entire temperature dependence term can be treated as a constant. It is important that the interaction energy in (5) can be negative which results in an anti-ferromagnetic coupling. The RKKY coupling field is [8],

$$H_{ex} = \frac{J_{ex}}{\mu_0 t_f M_f} = \frac{E_0}{t_f M_f (k_0 t_{Cu})^2} \sin(\frac{2\pi t_{Cu}}{\Lambda} + \psi) \frac{T/T_0}{\sinh(T/T_0)} \tag{8}.$$

RKKY coupling amplitude decreases substantially with interfacial roughness in Co/Cu/Co systems [16].

Pinhole coupling can also be important when interfacial roughness is considered. Difficult to model, pinhole coupling consists of “bridges” across the spacer layer that

allow for direct coupling between the two ferromagnetic layers. This kind of coupling is relevant when the spacer layer is thin and the amplitude of the roughness is large. It has a detrimental effect on GMR since the ferromagnetic layers can not switch independently and achieve an anti-parallel configuration.

Ignoring pinhole coupling the total coupling field between two ferromagnetic layers separated by a non-magnetic layer is [8],

$$H_{coup} = H_{ex} + H_{op} \qquad (9).$$

Magnetic couplings are important in understanding the effects of interfacial roughness on GMR.

2.5 Anisotropic Magnetoresistance

It is important to separate effects of anisotropic magnetoresistance (AMR) from those of giant magnetoresistance. AMR is observed in single ferromagnetic layers and is unrelated to the multilayer structure necessary for GMR. If the current is flowing parallel to the magnetic field applied an increase in resistance is observed with increasing magnetic field.

Measurements indicate that AMR can be described by the following equation,

$$\Delta\rho \cong A(1-e^{-\alpha|H|}) \qquad (10)$$

where A and α are parameters. With the magnetic field parallel to the current the deformed electron clouds offer more resistance to the current carrying electrons. There is a saturation level as the A parameter in (10) suggests.

The situation is different in the case of the current going perpendicular to the applied magnetic field. We have:

$$\Delta\rho_{\perp} \cong A_{\perp}(1-e^{-\alpha_{\perp}|H|}) \qquad (11).$$

In both cases the effect is rather small compared to GMR. The respective parameters in (10) and (11) have similar values and the sum of (10) and (11) is approximately zero which is confirmed by experimental data presented bellow.

2.6 Effects of Roughness

Roughness in GMR multilayers can have an effect on GMR through multiple channels. First of all, roughness can affect the magnetic properties of the ferromagnetic layers and the couplings between them as discussed previously.

Roughness can also have an effect on GMR through producing more scattering sites. If these sites produce more spin-dependant scattering, GMR will be enhanced.

However if the additional scattering leads to spin flipping it may decrease further spin dependent scattering and channeling resulting in a decrease in GMR.

Finally roughness can increase spin independent scattering which will lower the relative strength of the GMR effect. This will be observed as an increase of the overall resistivity of the sample. Additional spin independent scattering can decrease the mean free paths significantly resulting in higher resistivity. Intermixing of the multilayers as a result of roughness can further increase the overall resistivity of the samples. While this will not affect the difference in resistivity between the anti-parallel and the parallel states it will change its relative magnitude as compared to the overall resistivity of the sample.

3 Experiment

3.1 Rough Substrates

In order to introduce uniform roughness onto smooth substrates, we spin coat nanospheres, which are basically latex balls, of varying diameters onto standard 2" silicone wafers. Ideally this results in a single layer of nanospheres attached to the silicone substrate (see Figure 13). We used nonspheres with diameter 50,99,160,190,250,320,460 and 560nm. Two nanosphere sizes, 50nm and 460nm, are used for Co/Cu stacks and three samples are prepared for each nanosphere size listed above with the exchange biased spin valve structure.

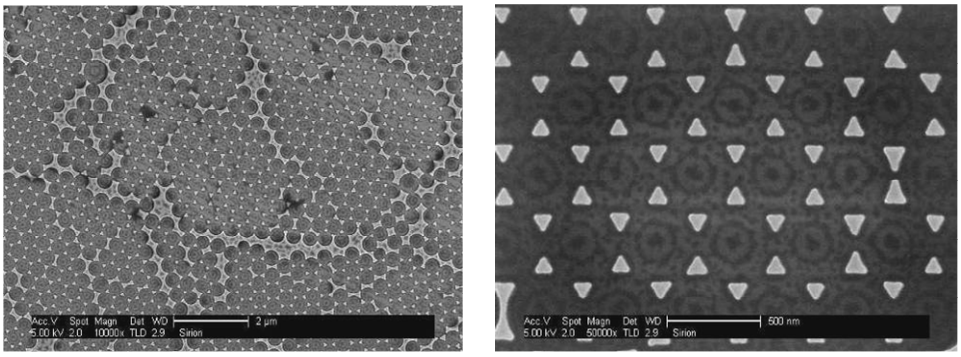

Figure 13. a) Polymer spheres on silicon substrate, b) Evaporated metal nanodot pattern. (Obtained from Dr. Jianjun Wang, AS William and Mary)

After spin coating the nanospheres, 15nm of Au is evaporated onto the sample. Au impinges on the substrate through the gaps remaining between the nanospheres. Then the substrate is placed in a difloromethane sonic bath for 10-15 minutes. This washes the nanospheres away and leaves Au "triangles" on the surface of the Si (Figure 13).

3.2 Giant Magnetoresistive Multilayers

Two different structures were used in this experiment, an exchange biased spin valve (ESBV) and a superlattice (many period) multilayer. The EBSV has the following structure: Nb3nm/Cu5nm/Co4nm/Cu4nm/Co4nm/FeMn10nm/Cu3nm/Nb2nm.
Niobium is used to facilitate crystalline growth on the substrate and to prevent oxidation. Notice that the FeMn, which is an anti-ferromagnetic material, is grown on the top of the structure. This is done in order to avoid unwanted effects of the substrate roughness on the pinning of the adjacent Co. Due to the anisotropic behavior of the pinned Co layer we can obtain both parallel and anti-parallel alignment of the two Co layers depending on the external magnetic field. The second structure which is studied in much less detail is a Co/Cu multilayer.

The multilayers have the following structure: Nb3nm/[Cu5nm/Co4nm]x10/Cu10nm/Nb2nm. Niobium serves the same purpose as in the EBSV. RKKY coupling is responsible for GMR in this structure. Recall that (5) suggests that the Co layers can be coupled antiferromagnetically. This is the case with the Co/Cu multilayer. As the external field increases some of the Co layers switch and align themselves with the external field as their neighboring anti-ferromagnetically coupled Co

layers remain magnetized opposite to the field resulting in high resistance. As the field increases further the anti-ferromagnetic coupling is overcome and all the layers align with the magnetic field resulting in lower resistance.

The ½ x ½" films grown for this experiment were produced by sputtering in a vacuum chamber at Michigan State University. The vacuum chamber was initially evacuated to a pressure of about 1 x 10^{-9} Torr and then the polycrystalline films were grown at room temperature in argon gas at a pressure of roughly 1 mTorr. The EBSV samples were pinned by heating them to 180°C and then cooling them in a uniform magnetic field.

3.3 Giant Magnetoresistive Measurements

For the GMR measurements, the samples are placed in a holder between the poles of an electromagnet (GMW 3470 Electromagnet, driven by Kepco BOP 50-4D 4886 bipolar power supply) which provides the applied magnetic field.

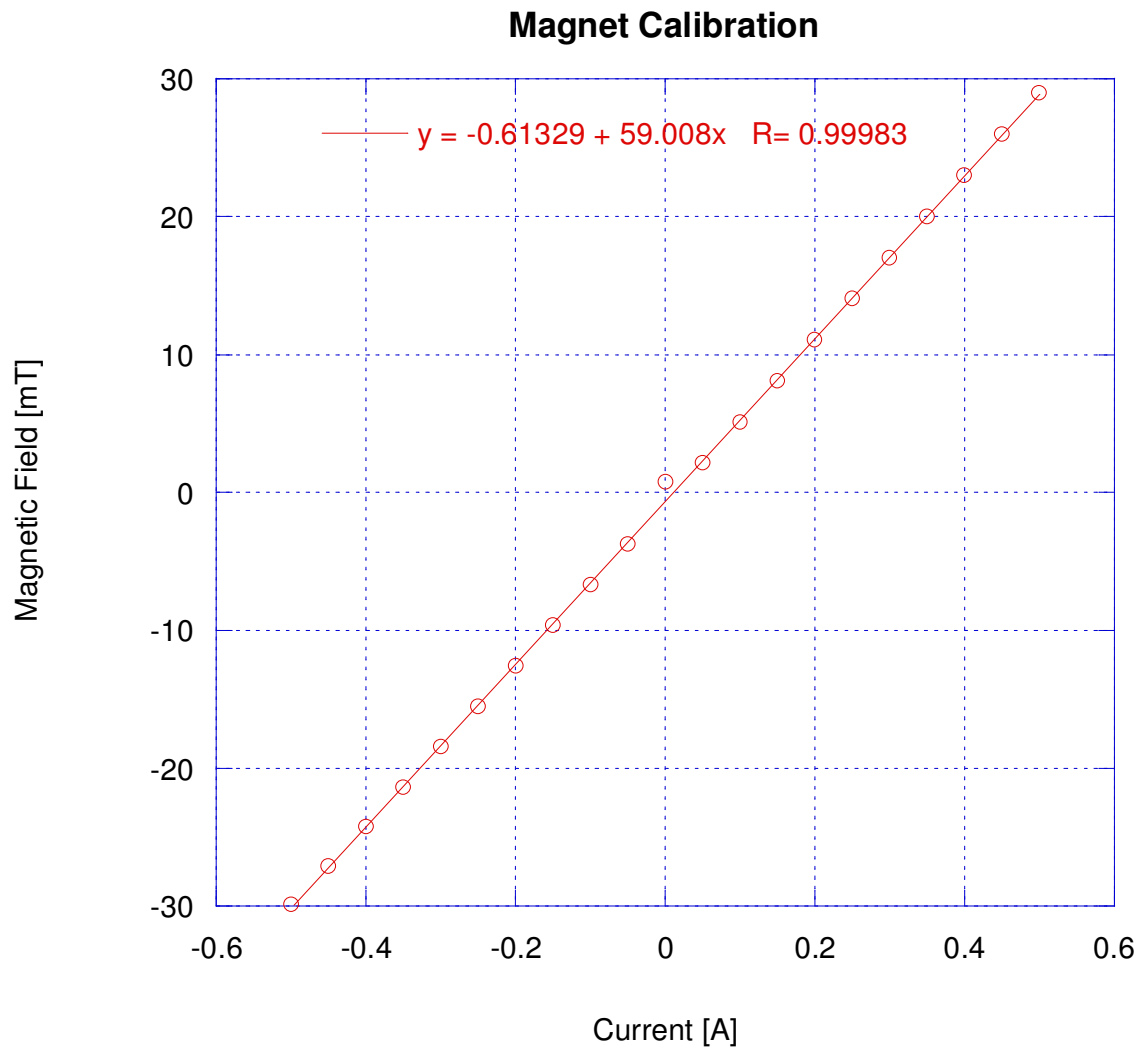

Figure 14. Magnetic Field as a function of applied field.

Let us first consider magnet calibration. Figure 14 shows the measured field as a function of the applied current. As expected the fit is linear but there is a slight offset at zero field due to coercivity of the magnet and Earth's magnetic field.

A custom built 4-point probe sample holder is used, for resistance measurements, which eliminates the need for solder joints. The sample stage supplies four connections with the circumference of the sample through Pogo-25B-6 gold plated contacts. The

resistance is measured by applying a constant current along one edge of the sample and measuring the voltage drop across the other parallel edge. A Keithley 4ZA4 Sourcemeter provides the current (10 mA) through the sample via two of the four contacts. A HP3401A multimeter measures the voltage drop along the other two contacts. We use a computer running LabView to drive the experiment and record the data. Two measurements are made for each sample so that we can compute resistivity with the van der Pauw method. Maximum field is held for 5 seconds to ensure proper initial magnetization and then is cycled down to a minimal value and back. Each of the three EBSV samples for each nanosphere sizes is measured separately.

We used the van der Pauw method for measuring and calculating resistivity [10]. There are some conditions that must be satisfied for this approach to work: contacts must be at the circumference of the sample; contacts must be sufficiently small; sample must be homogeneous in thickness; and surface of the sample must be singly connected.
When these conditions are satisfied, the following equation gives the resistivity,

$$\rho = \frac{\pi d}{\ln(2)} \frac{R_{AB,CD} + R_{BC,DA}}{2} f(R_{AB,CD} / R_{BC,DA}) \qquad (12).$$

In equation (12) ρ is the resistivity, d is the thickness of the sample, $R_{AB,CD}$ is the voltage drop along AB divided by the current flowing through CD and $R_{BC,DA}$ is the voltage drop along BC divided by the current flowing through DA. A, B, C and D are the points of contact along the circumference of the sample. Note that in (12) we are taking an average of the resistance measured parallel and perpendicular to the field which will average out the AMR in the final resistivity value.

The function f is determined by

$$\frac{R_{AB,CD} - R_{BC,DA}}{R_{AB,CD} + R_{BC,DA}} = ar\cosh\left(\frac{e^{\frac{\ln 2}{f}}}{2}\right) f \qquad (13).$$

Unfortunately this transcendental equation is not very useful. A good approximation when $R_{AB,CD} \cong R_{BC,DA}$ is

$$f \cong 1 - \left(\frac{R_{AB,CD} - R_{BC,DA}}{R_{AB,CD} + R_{BC,DA}}\right)^2 \frac{\ln 2}{2} - \left(\frac{R_{AB,CD} - R_{BC,DA}}{R_{AB,CD} + R_{BC,DA}}\right)^4 \left(\frac{(\ln 2)^2}{2} - \frac{(\ln 2)^3}{12}\right) \qquad (14).$$

The error in the power series expansion in (14) does not exceed

$$\left(\frac{R_{AB,CD} - R_{BC,DA}}{R_{AB,CD} + R_{BC,DA}}\right)^4 \left(\frac{(\ln 2)^2}{2} - \frac{(\ln 2)^3}{12}\right) \qquad (15).$$

So with the above equations in mind we can obtain the resistivity of a sample from two perpendicular resistance measurements.

The following paragraphs briefly discuss how data is extracted from the GMR plots. We can measure coercivity of the free (H_{CF}) and pinned layers (H_{CP}), maximum (ρ_{max}) and minimum resistivity (ρ_{min}) of the sample, exchange biasing (H_{EB}) of the pinned layer and coupling between the ferromagnetic layers (H_{COUP}). While some of the quantities are apparent from the graph some require an explanation. The pinned layer will switch away from zero field due to its exchange bias, while the free layer switches near zero field. Any offset of the switching of the free layer is the effect of coupling between the two ferromagnetic layers. Maximum and minimum resitivities are easily obtained from the curve and GMR% is calculated by

$$GMR_{\%} = \frac{\rho_{\max} - \rho_{\min}}{\rho_{\min}} \qquad (16).$$

We can obtain the coercivities, exchange bias and coupling field as shown in Figure 15. The measurements of all the magnetic properties are made at $\frac{\rho_{\max} + \rho_{\min}}{2}$.

GMR plots of exchange biased spin valves (EBSV) contain sections that look like parts of hysteresis loops. In an EBSV one Co layer is pinned with the help of FeMn and the other is left "free" to rotate magnetization which allows for the desired anti-parallel alignment. The fields at which the pinned and free layers switch are different depending on their previous magnetization. Going through Figure 15, we start on the right, with both layers magnetized to the right. As the field decreases, the pinned layer under the influence of the adjacent anti-ferromagnetic switches magnetization to the left. This happens at $H_{EB} - H_{CP}$. This results in the anti-parallel alignment and a sharp increase in

GMR as the switch occurs. Then as the field further decreases the free layer also switches to the left at H_{COUP} - H_{CF} resulting in parallel alignment and decrease in GMR. On the way back as the field increases, the free layer switches to the right, this time at H_{COUP} + H_{CF}, resulting in anti-parallel alignment and again increase in GMR. At H_{EB} + H_{CP} the pinned layer switches again to the right resulting in a decrease in GMR. So without any explicit hysteresis loop measurements we can obtain most important magnetic properties of both layers. Unfortunately we can not obtain anything more than the resistivity from the Co/Cu stacks used in a part of this experiment.

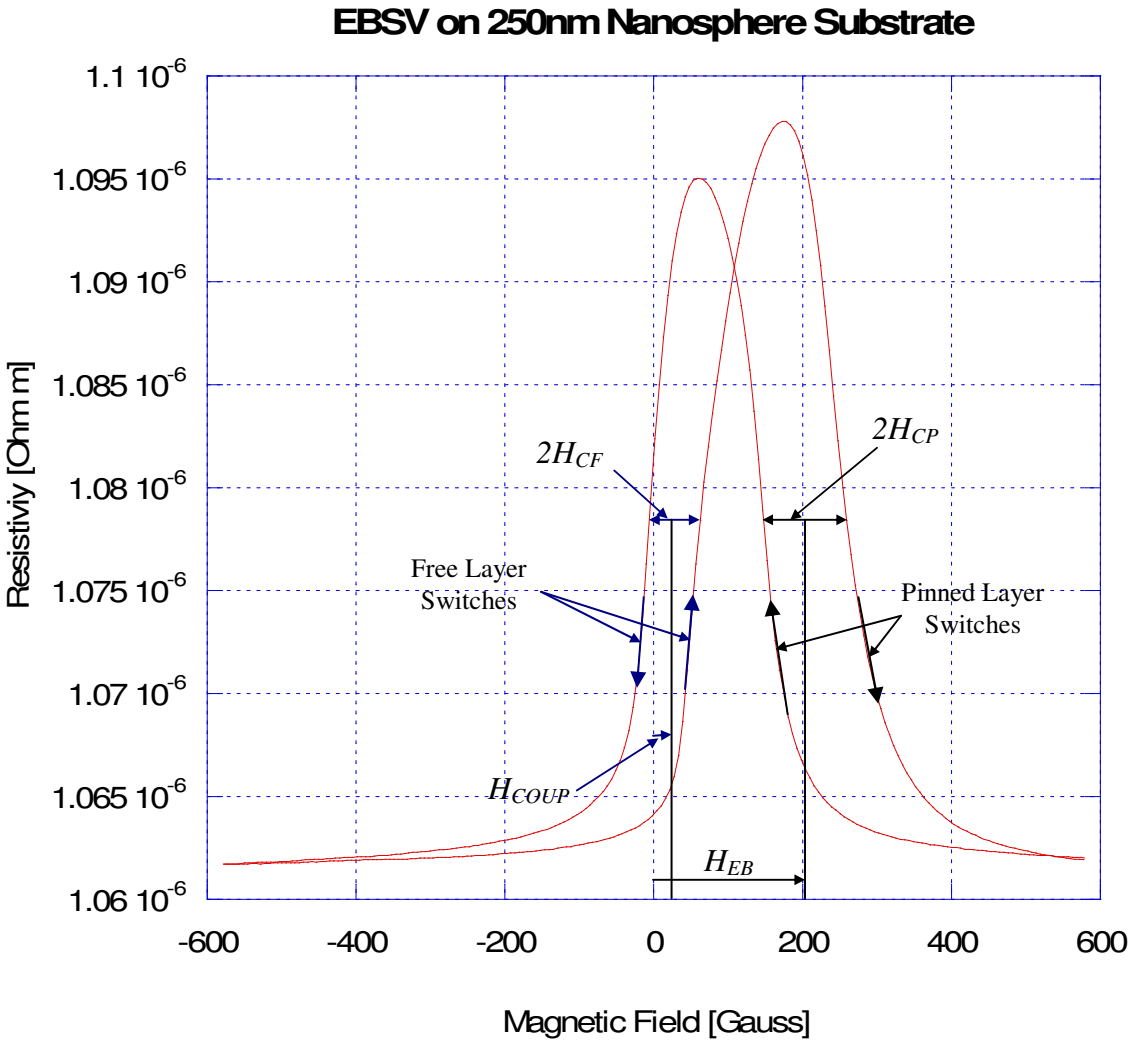

Figure 15. Reading off coercivities, exchange bias, coupling field and resistivity from an EBSV curve.

3.4 Roughness Measurements

Finally we measure and characterize the roughness with a Nanoscope Scanning Probe microscope at the Applied Research Center at Jefferson Lab. Three 1μm by 1μm measurements are made on each Co/Cu stack and one per EBSV sample, since there are three EBSV samples for each nanosphere size.

Figure 16 shows a schematic description of how an atomic force microscope (AFM) works. In our measurements the AFM works in tapping mode which means that it touches the surface of the sample at the very bottom of its oscillation. This affects the oscillation and the change is detected through photodetecting a laser beam reflected off of the oscillating cantilever. Analyzing the changes in oscillation allows the computer to produce a topographical map of the sample.

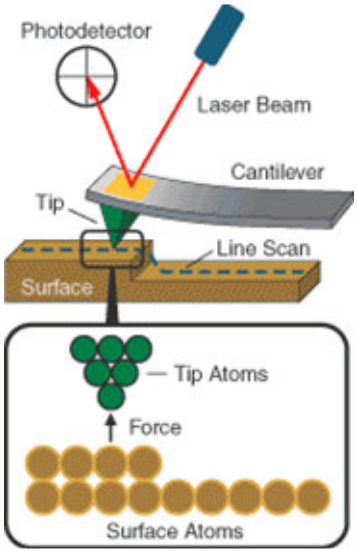

Figure 16. A schematic depicting the basic principle behind the operation of an atomic force microscope.

(Obtained from http://www.molec.com/media/images/AFM-Schematic.gif)

Since only $3\mu m^2$ are scanned, if the samples have non uniform roughness we are not going to get a good representation of the average roughness and the error bars are going

to be high. This would not be a problem if we get the anticipated uniform nanodot pattern.

3.5 A Note on Error Bars

All measurement errors and error bars presented in this thesis are standard errors in the mean. The relationship between the standard error in the mean and a standard deviation is,

$$SEM = \frac{\sigma}{\sqrt{N}} \tag{17}$$

where *SEM* is the standard error in the mean, σ is the standard deviation and N is the number of measurements. *SEM* propagates in the same manner as σ. *SEM* gives us 95% confidence that the actual mean is within an *SEM* from the measured mean.

4 Results

4.1 Co/Cu Multilayer Data and Analysis

Co/Cu multilayers were studied to see the effects of substrate roughness on a system with multiple interfaces. Table 1 summarizes the measurements. Unfortunately the desired nanodot pattern was not observed in any of the Co/Cu samples due to difficulties with spin coating a single layer of nanospheres onto the Si. Figure 17 shows the second AFM scan for the 50nm nanospheres. The other scans look similar. Some of

the scans also suggest that the nanospheres were not completely removed by the difloromethane. While the desired structure is not present some Au still found its way onto the Si and non-uniform roughness is observed as the data in Table 1 suggests. Unfortunately this also means large error bars since the roughness is non-uniform.

Structure	RMS Roughness [nm]	Standard Error in Roughness [nm]	ρ_{min} [Ohm m]	ρ_{max} [Ohm m]	GMR [%]
Reference	2.8407	0.5286	9.721e-8	1.0623e-7	9.2836
50nm	4.6590	0.665617	1.3012e-7	1.3745e-7	5.6309
460nm	10.602	3.189747	1.2977e-7	1.3625e-7	4.9919

Table 1. Summary of Co/Cu multilayer data. GMR % decreases with roughness.

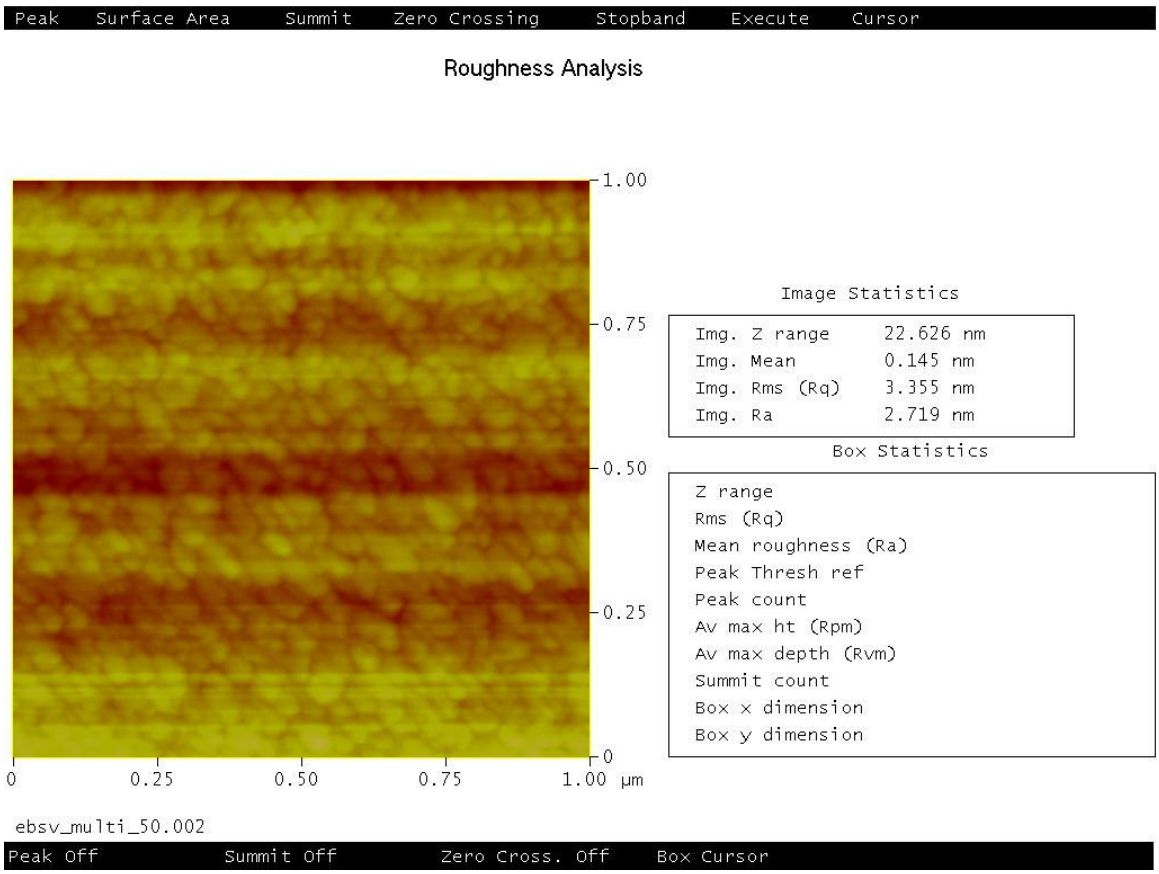

Figure 17. Co/Cu 50nm nanosphere, AFM scan. No nanodots unfortunately which suggests more then one layer of nanospheres was spin coated.

Errors associated with the resistivity calculations are listed in Table 2. These are minor and have no significant effect on the data. The f_{err} comes directly from equation (15) and is a consequence of the difference of resistance along and perpendicular to the applied field. B_{diff} is the difference in actual field between any two points used for computing the resistivity. While the current set points are the same in both plots the actual current measured and resulting field varies somewhat between measurements. Both B_{diff} and f_{err} are the maximum values of all the plot points. Figures 18, 19 and 20 show the original resistance plots and the calculated resistivity plot for Co/Cu bare substrate respectively.

Structure	f_{err} [%]	B_{diff} [G]
Reference	.024	.73
50nm	.014	1.1
460nm	.003	.37

Table 2. Summary of errors in ρ calculations. Both numbers are maximums from the calculations of all points (about 400 per plot).

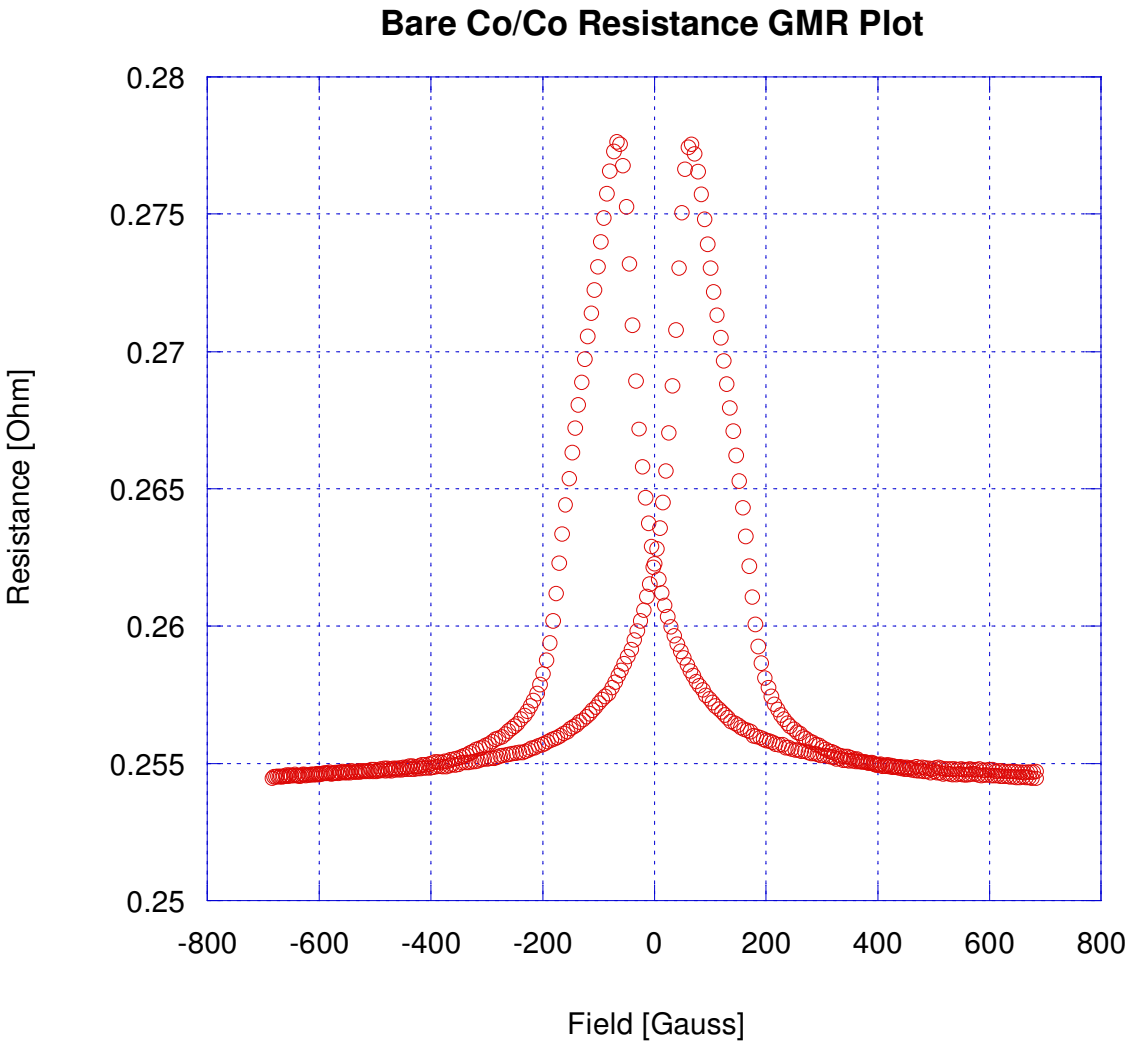

Figure 18. Voltage drop divided by applied current measured perpendicular to the field.

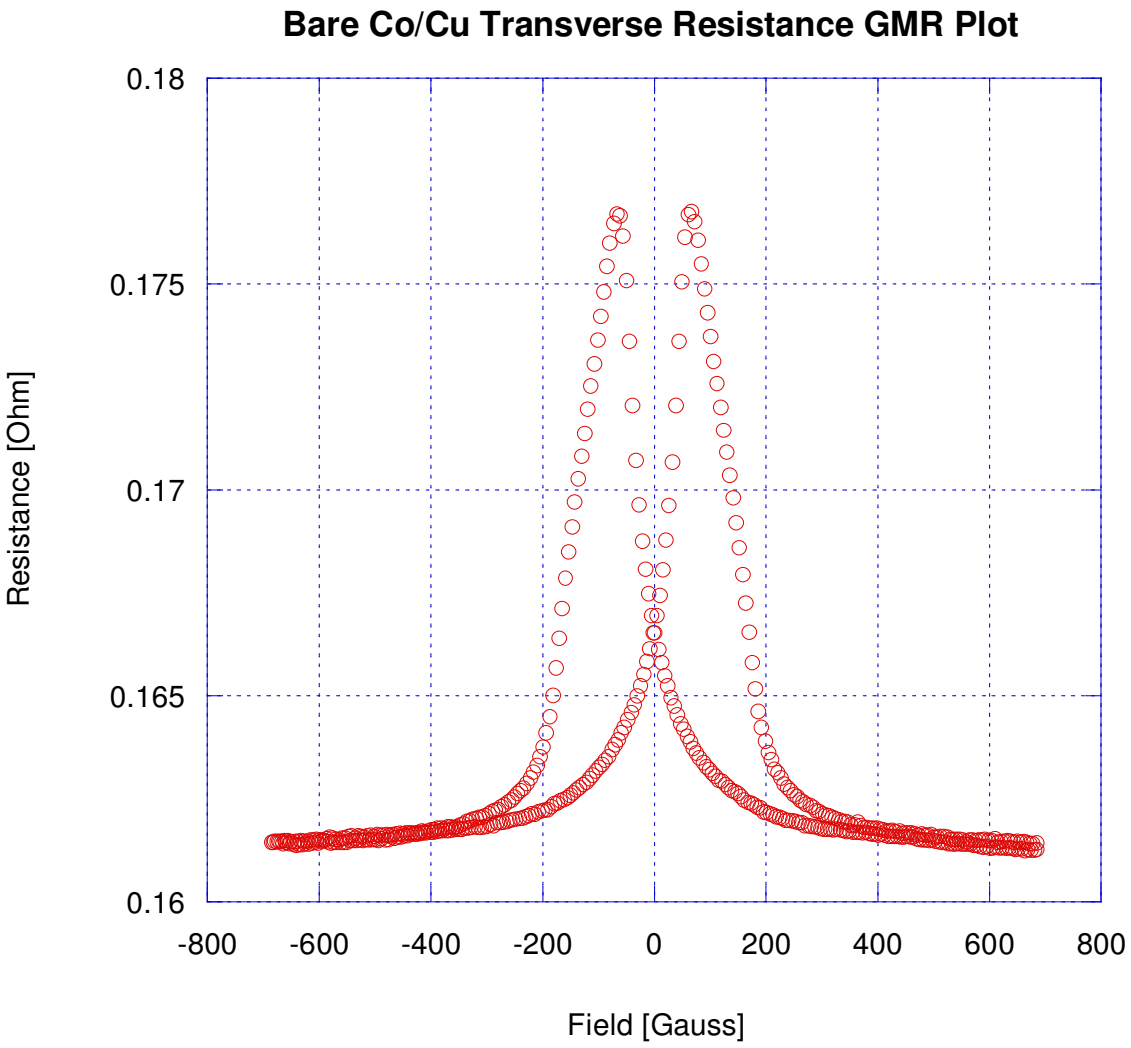

Figure 19. Voltage drop divided by applied current measured parallel to the field.

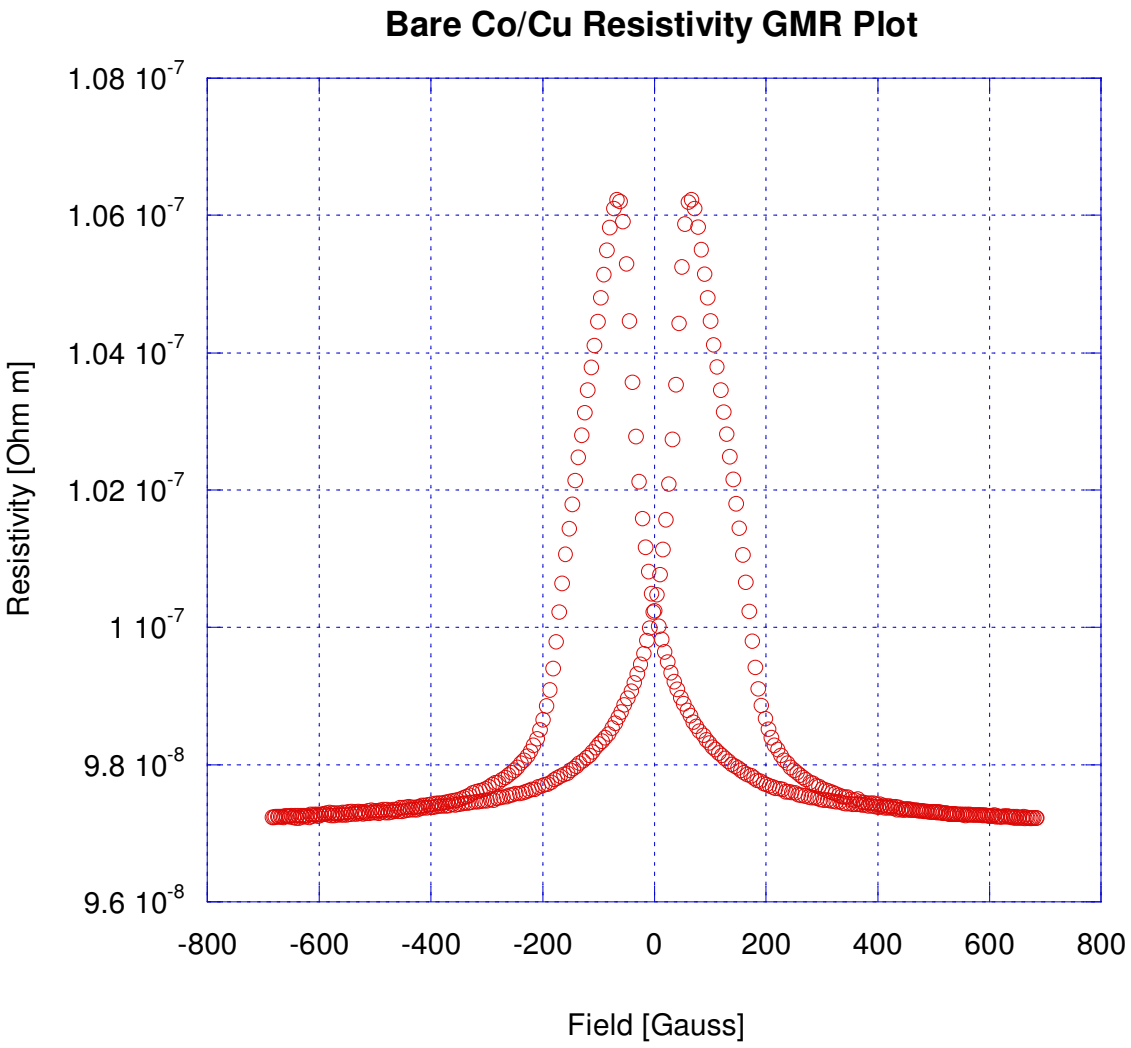

Figure 20. Calculated resistivity for Co/Cu stack on a bare substrate.

Note the slight effects of AMR on the GMR plots in Figures 18 and 19 near zero field. These do not affect the measurements in Table 1 and are not even noticeable when averaged out in Figure 20.

Table 1 suggests most of the decrease in GMR comes from the increased sample resistivity with increasing roughness. The difference between maximum and minimum resistivity is on average about .076 10^{-8} Ωm. A contributing factor to that decrease in GMR is also the slight decrease in the difference between maximum and minimum

resistivity coming most likely from orange peel magnetic coupling between the layers and decreasing RKKY antiferromagnetic coupling. In a Co/Cu multilayer the antiparallel alignment is heavily dependent on the magnetic couplings and their effect on GMR is noticeable. Unfortunately there is no way to obtain these magnetic properties from the GMR plots.

4.3 EBSV Data

EBSV were used because in this structure a true anti-parallel state can be achieved. The majority of data for this experiment came from the EBSVs for two reasons. There are 27 EBSV samples with 8 different nanosphere sizes used compared to 3 Co/Cu samples with 2 nanosphere sizes used. Second there are a number of magnetic properties that we can obtain from the GMR plots of EBSV that are unavailable in Co/Cu GMR plots. Let us start by analyzing the roughness data.

4.3.1 EBSV Roughness Data

Unfortunately out of 27 EBSV structures only 2 showed the desired nanodot structure. Data from the third 320nm nanosphere EBSV sample is shown in Figures 21 and 22.

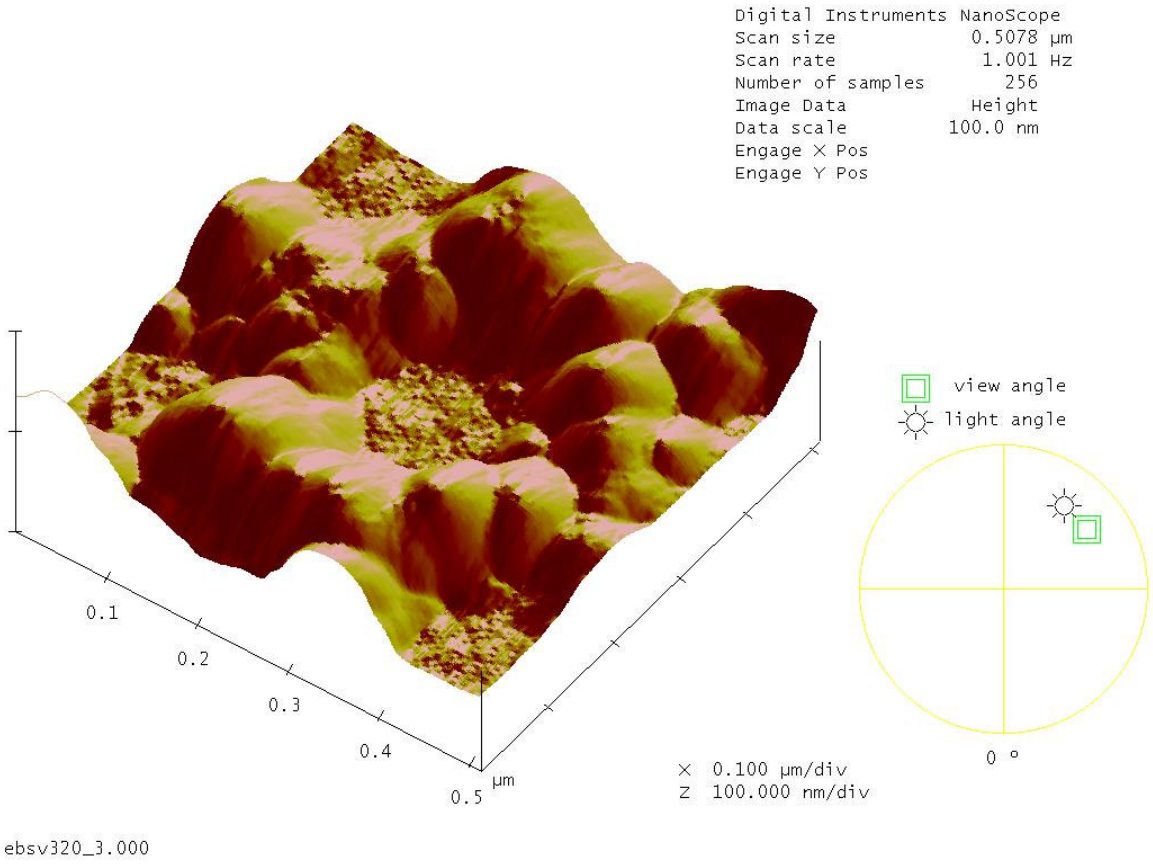

Figure 21. 3D image of the EBSV deposited on top of the nanodot pattern obtained from a 320nm nanospheres.

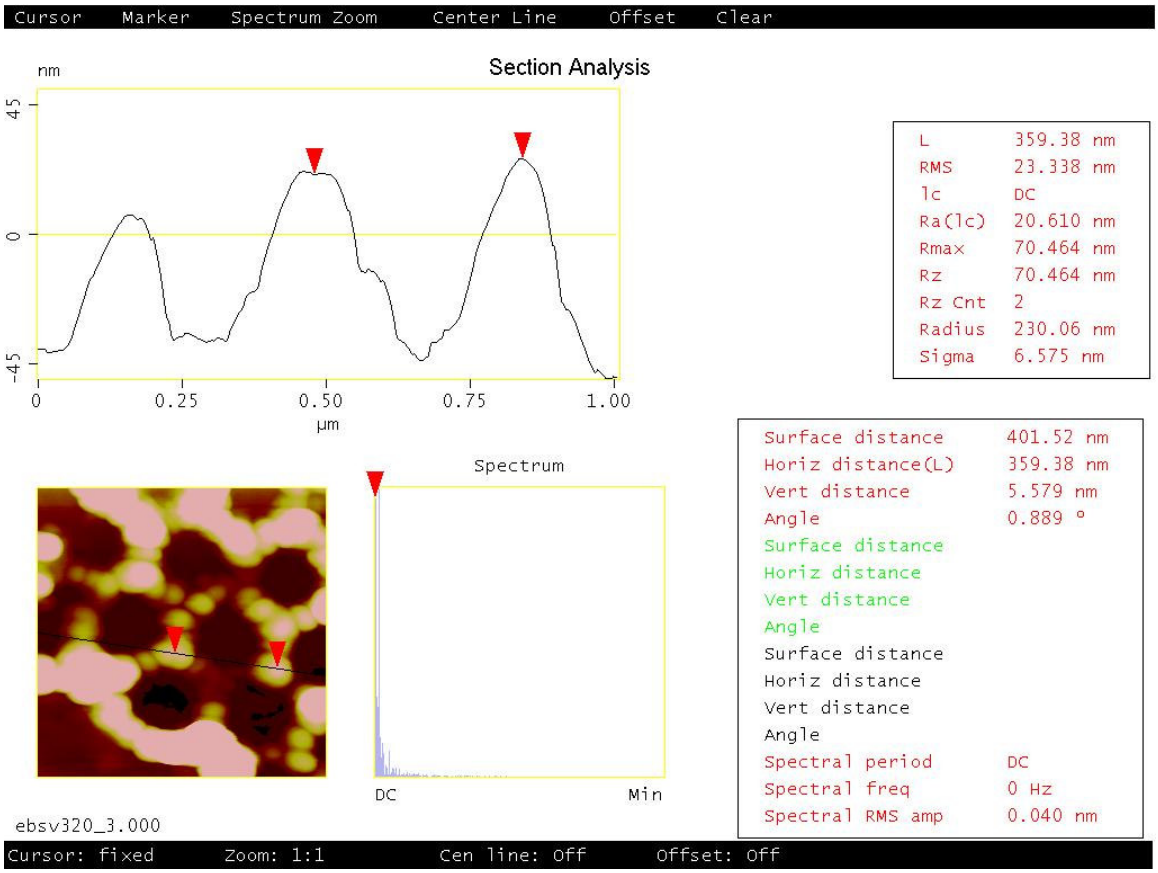

Figure 22. Sectional analysis of the EBSV deposited on top of the nanodot pattern obtained from a 320nm nanospheres. Horizontal spacing is slightly larger then expected at 359.38nm but not unreasonable.

Data from the 560nm nanospheres AFM scans is shown in Figures 23 and 24.

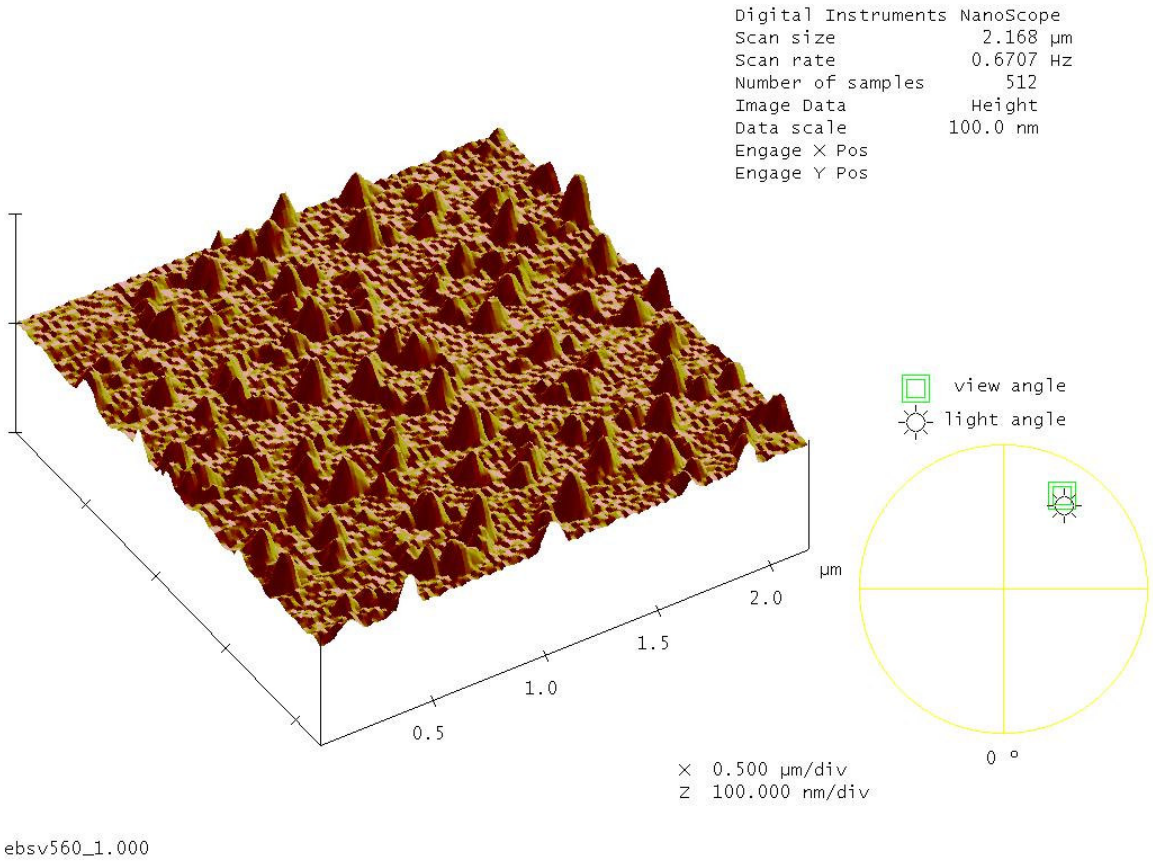

Figure 23. 3D image of the EBSV deposited on top of the nanodot pattern obtained from a 560nm nanospheres.

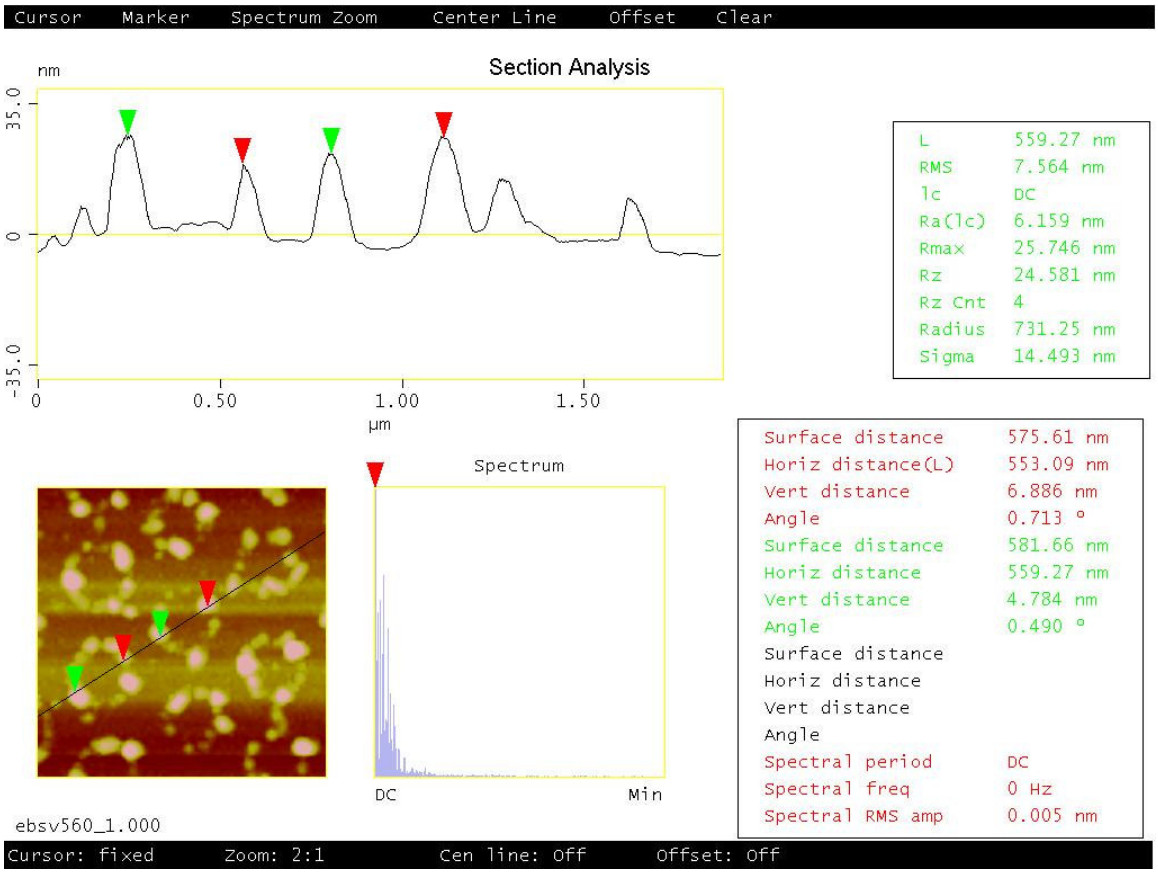

Figure 24. Sectional analysis of the EBSV deposited on top of the nanodot pattern obtained from a 560nm nanospheres. Horizontal spacing is slightly smaller then expected at 553.09 nm.

The cross sections show that we are indeed looking at the nanodots. Data from the other samples is used but is highly non-uniform resulting in large error bars. Table 3 shows the AFM results from all EBSV samples.

Structure	RMS Roughness [nm]	Standard Error [nm]
Reference	4.4887	1.2602
50nm	4.6590	0.66562
99nm	7.3997	0.75684
160nm	10.981	4.9574
190nm	6.8183	2.4014
250nm	12.026	4.8637
320nm	17.064	9.1586
460nm	9.5060	2.3420
560nm	20.341	7.2914

Table 3. RMS Roughness of the EBSV samples.

Notice that the lower the roughness the lower the error in Table 3. This is to be expected as the low RMS roughness suggests that little Au made its way onto the substrate and therefore the surface is relatively uniform.

4.3.2 Resistivity Calculations and Magnetic Properties of EBSV Samples

Table 4 lists the errors associated with the resistivity calculations. These are again minor and average out in the calculation of the standard error in the mean for each of the quantities.

Structure	f_{err} [%]	B_{diff} [G]
Reference	0.049517	0.654485
50nm	0.059088	0.695945
99nm	0.109344	0.450143
160nm	0.039454	0.530103
190nm	0.306787	0.245802
250nm	0.151169	0.571564
320nm	0.154781	0.571564
460nm	0.206782	0.530103
560nm	0.060368	0.533065

Table 4. Errors associated with the resistivity calculation. The error in f is due to an approximation in the van der Pauw method and the difference in field comes from the measurements.

Figures 25, 26 and 27 show the resistance, transverse resistance and resistivty curves for the 560nm nanosphere EBSV sample.

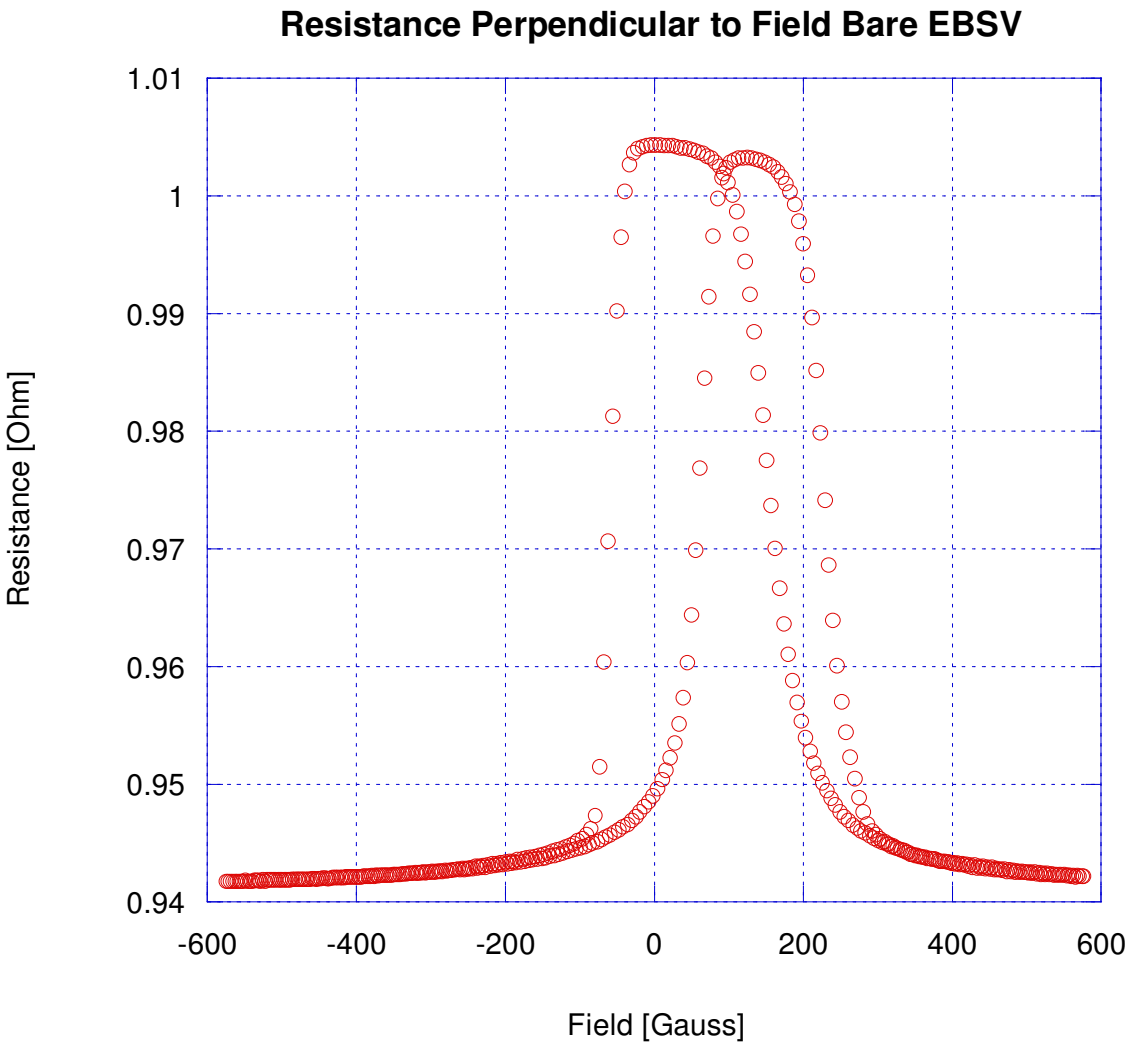

Figure 25. Resistance perpendicular to field for reference EBSV sample. Notice that the peak around zero is higher then the other one due to AMR.

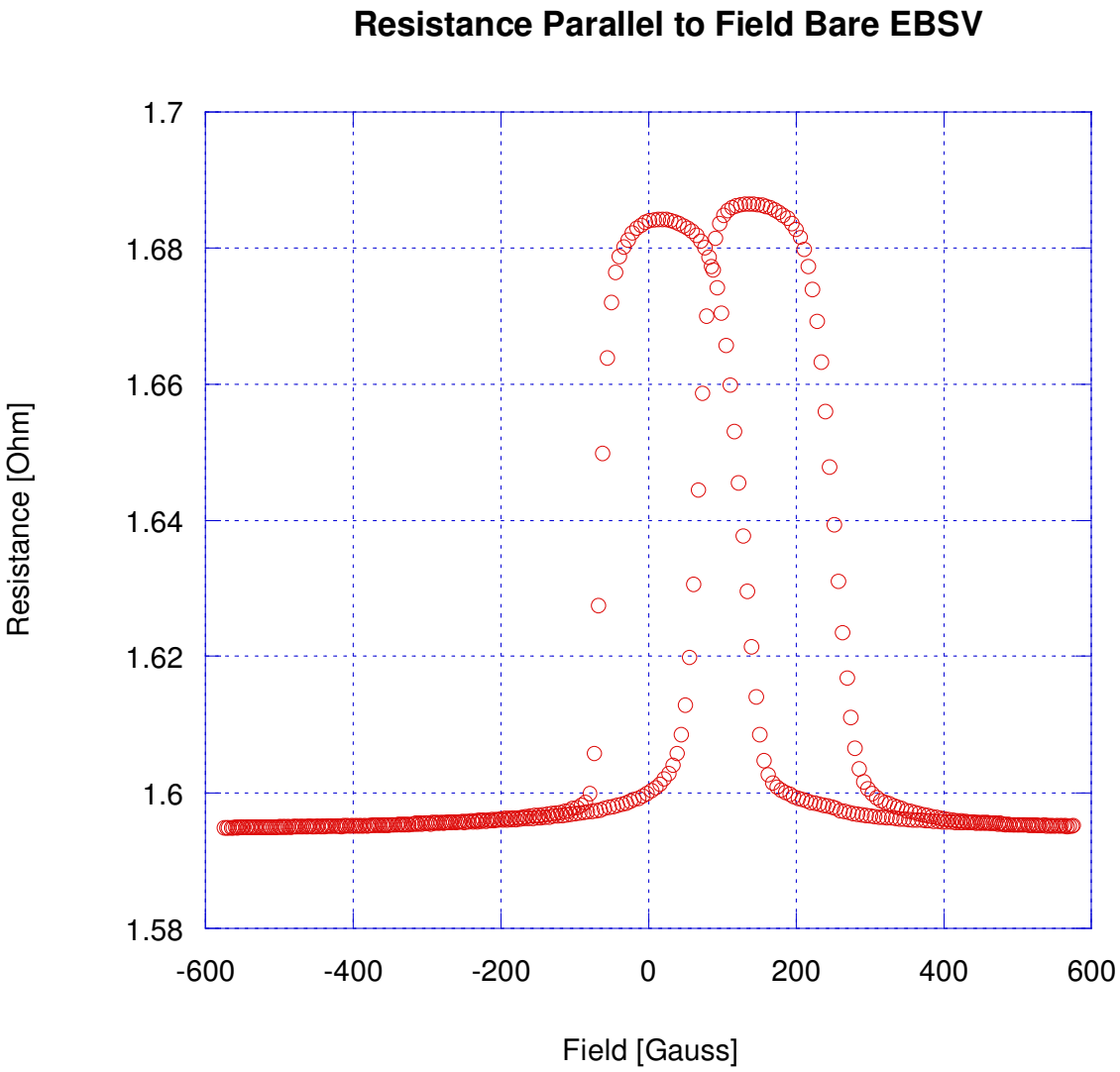

Figure 26. Resistance parallel to field for reference EBSV sample. Notice that the peak around zero is lower then the other one due to AMR.

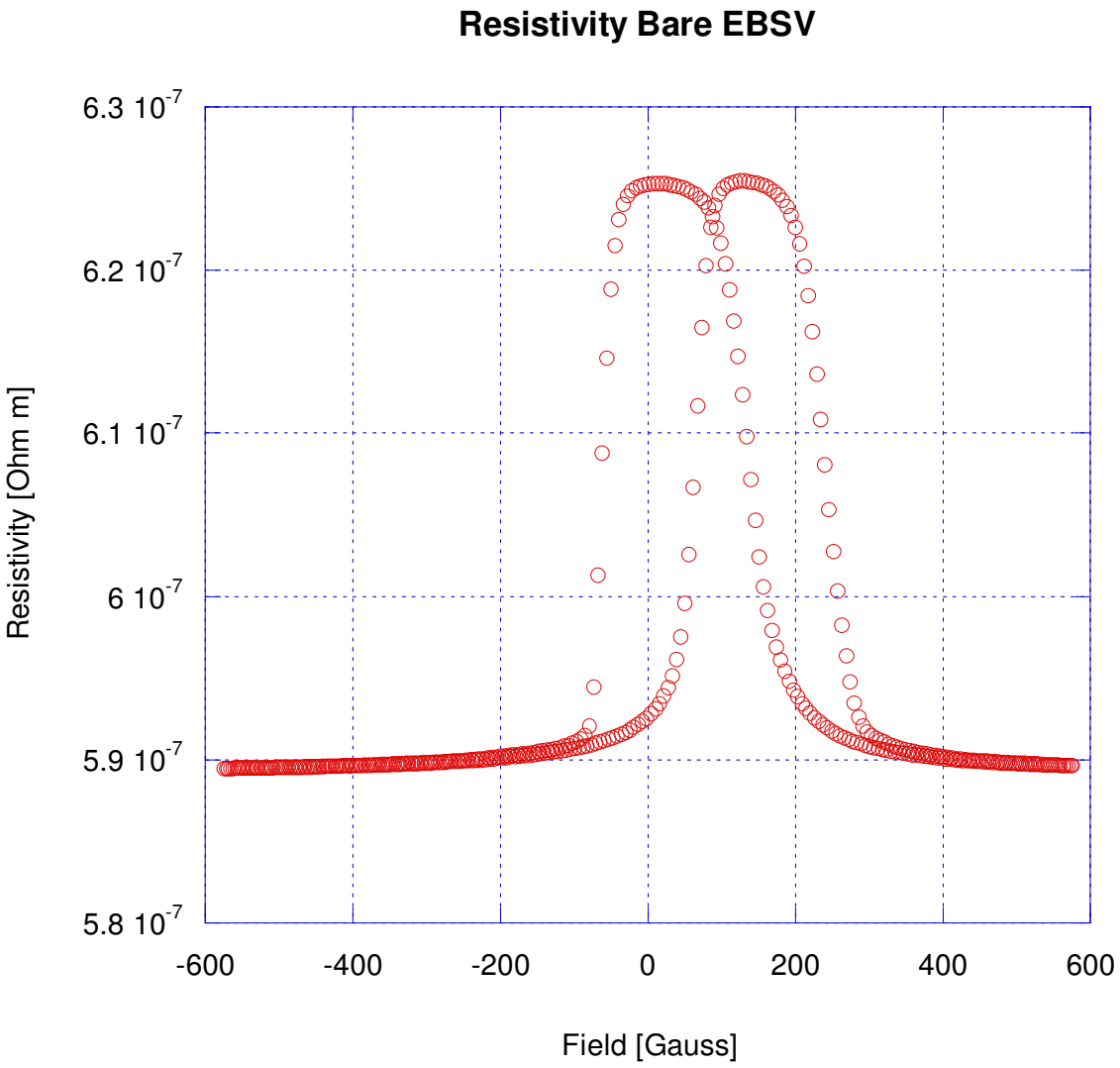

Figure 27. Calculated resistivity plot for reference EBSV sample. Notice that the peak around zero the same height as the other peak.

One important thing is apparent from Figures 25, 26 and 27, AMR indeed cancels out as expected. The peak around zero is about the same height as the other one in the resistivity plot which is not the case in the resistance plots.

One advantage of the EBSV is that we can extract a multitude of data on the magnetic properties of the structure from the GMR plot. Table 5 lists these.

Structure	H_{CF} [G]	H_{CF}^{Error} [G]	H_{PF} [G]	H_{PF}^{Error} [G]	H_{EB} [G]	H_{EB}^{Error} [G]	H_{Coup} [G]	H_{Coup}^{Error} [G]
Reference	54.604	4.1903	49.707	3.0270	197.05	5.2107	1.2180	0.84141
50nm	32.053	1.5165	49.447	1.8420	197.63	3.2108	25.313	1.0488
99nm	38.793	3.5542	60.162	5.9052	181.47	3.7360	49.797	3.8542
160nm	39.538	2.7561	58.581	4.7944	189.34	12.578	49.589	4.2674
190nm	36.012	2.0703	60.781	1.9994	199.32	5.4356	51.427	2.9318
250nm	33.988	1.9521	54.955	2.6710	194.07	5.6153	32.233	1.8601
320nm	58.805	5.9739	89.112	3.8419	191.70	0.92626	24.742	5.2832
460nm	30.367	1.7135	42.067	3.0050	192.30	3.3697	18.588	1.9877
560nm	32.784	1.0188	47.773	5.1539	209.22	4.1477	20.590	3.4919

Table 5. Magnetic properties of the EBSV samples and their respective errors.

The data in Table 5 confirms that the exchange bias is for all intensive purposes unaffected by the roughness. This was the idea behind depositing the FeMn on top of the structure. Coercivities of the free and pinned layers vary significantly due to domain structure changes and couplings associated with the roughness. Coupling field varies quite a bit as well due to orange peel, RKKY and pinhole couplings. Data is obtained through linear interpolation and errors are the standard errors in the mean based on the three samples for each nanosphere size. Further analysis of the data follows bellow.

4.3.3 Electric Properties of EBSV Samples

Data on the electric properties of the EBSV samples is presented in this section. Table 6 contains all the relevant quantities and their errors.

Structure	ρ_{min} [μΩcm]	ρ_{min}^{Error} [μΩcm]	ρ_{max} [μΩcm]	ρ_{max}^{Error} [μΩcm]	$\Delta\rho$ [μΩcm]	$\Delta\rho^{Error}$ [μΩcm]	GMR [%]	GMR^{Error} [%]
Reference	5.9850	.046403	6.3448	.046666	.35976	.0018016	6.0116	0.045983
50nm	13.864	.79370	14.184	.78942	.32017	.032410	2.3295	0.21522
99nm	16.714	1.3092	17.096	1.3523	.38259	.079673	2.2773	0.11704
160nm	19.270	.63144	19.682	.64321	.41178	.061476	2.1381	0.17649
190nm	14.318	.33040	14.579	.32004	.26079	.071718	1.8277	0.31095
250nm	9.8973	.37090	10.234	.38222	.33716	.020550	3.4077	0.040402
320nm	18.150	.70702	18.362	.70535	.21283	.025995	1.1771	0.097875
460nm	7.7223	.29600	8.0561	.29622	.33376	.0058756	4.3341	0.16360
560nm	8.3776	.40108	8.7504	.39783	.37278	.025223	4.4752	0.30948

Table 6. Electric properties of EBSV samples and associated errors.

The decrease in GMR is proportional to the increase in overall resistivity and no significant changes are observed in $\Delta\rho$. The resistivity values are very reasonable compared to the resistivity of Co 15μΩcm and Co 3 μΩcm for the bulk materials.

4.4 EBSV Data Analysis

Let us look at some plots of the data listed above and explore the relationships between the quantities. First let us look at a plot of the GMR% versus minimum resistivity (Figure 28). GMR% is by definition,

$$GMR\% \equiv \frac{\rho_{\max} - \rho_{\min}}{\rho_{\min}} \equiv \frac{\Delta\rho}{\rho_{\min}} \qquad (18).$$

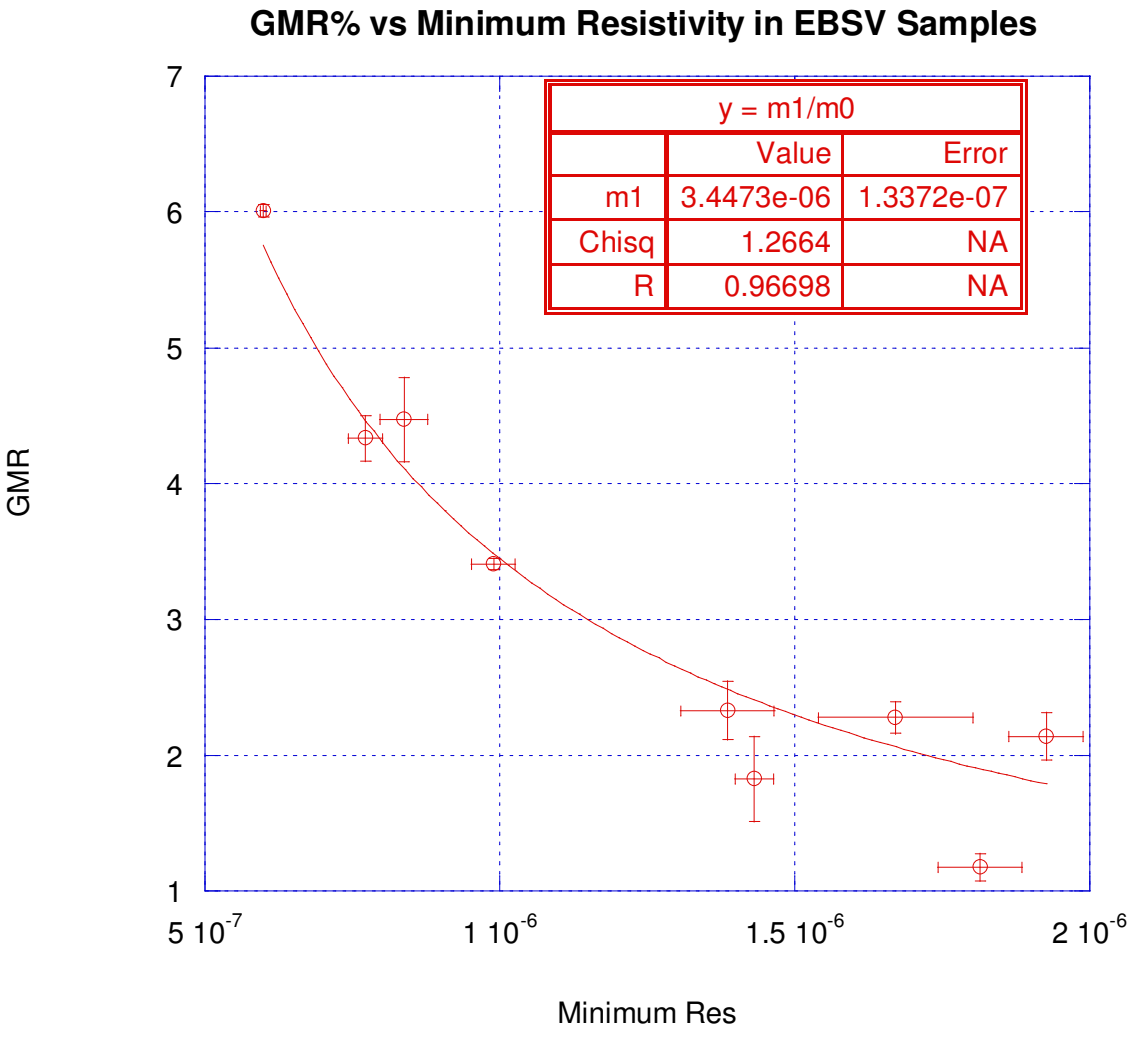

Figure 28. A plot of the GMR% vs. minimum resistivity.

So assuming constant $\Delta\rho$ we would have a $1/\rho_{min}$ relationship. This seems to be the case in Figure 28 with $\Delta\rho = .3447 \pm .0134\ \mu\Omega cm$. This is in excellent agreement with the data in Table 6 suggesting that the effects on GMR are indeed dominated by the effects of roughness on overall resistivity. To further confirm this point let us look at the plot of the maximum resistivity vs. minimum resistivity in Figure 29.

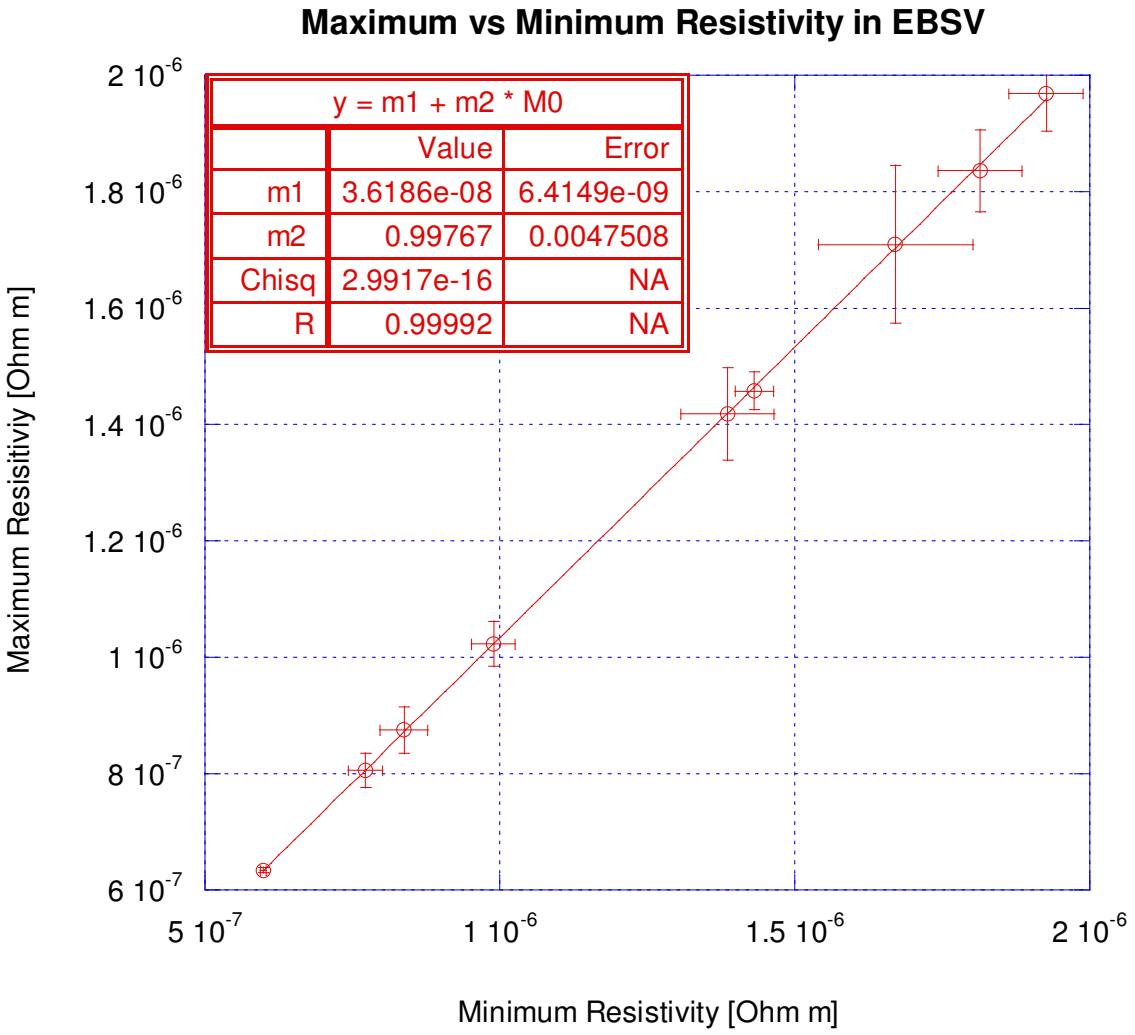

Figure 29. Maximum resistivity vs. minimum resistivity in EBSV samples.

The slope is, within the error, equal to 1. This is exactly what we would expect if overall resistivity was solely responsible for the changes in GMR. The y-intercept is simply $\Delta\rho =$

$.3619 \pm .0641\ \mu\Omega cm$ in excellent agreement with the value obtained in Figure 28 and the data in Table 6.

With this in mind let us look at the effects of roughness on resistivity and GMR. Figure 30 suggests a weak oscillatory relation between roughness and resistivity. It would be difficult to model this with confidence due to the large errors in the roughness measurements. It is safe to say that the first drop in GMR% is most likely the result of decreased channeling. With roughness at the interfaces we do not expect any significant channeling to occur in the Cu layer which results in a sharp increase in the resistivity and decrease in GMR.

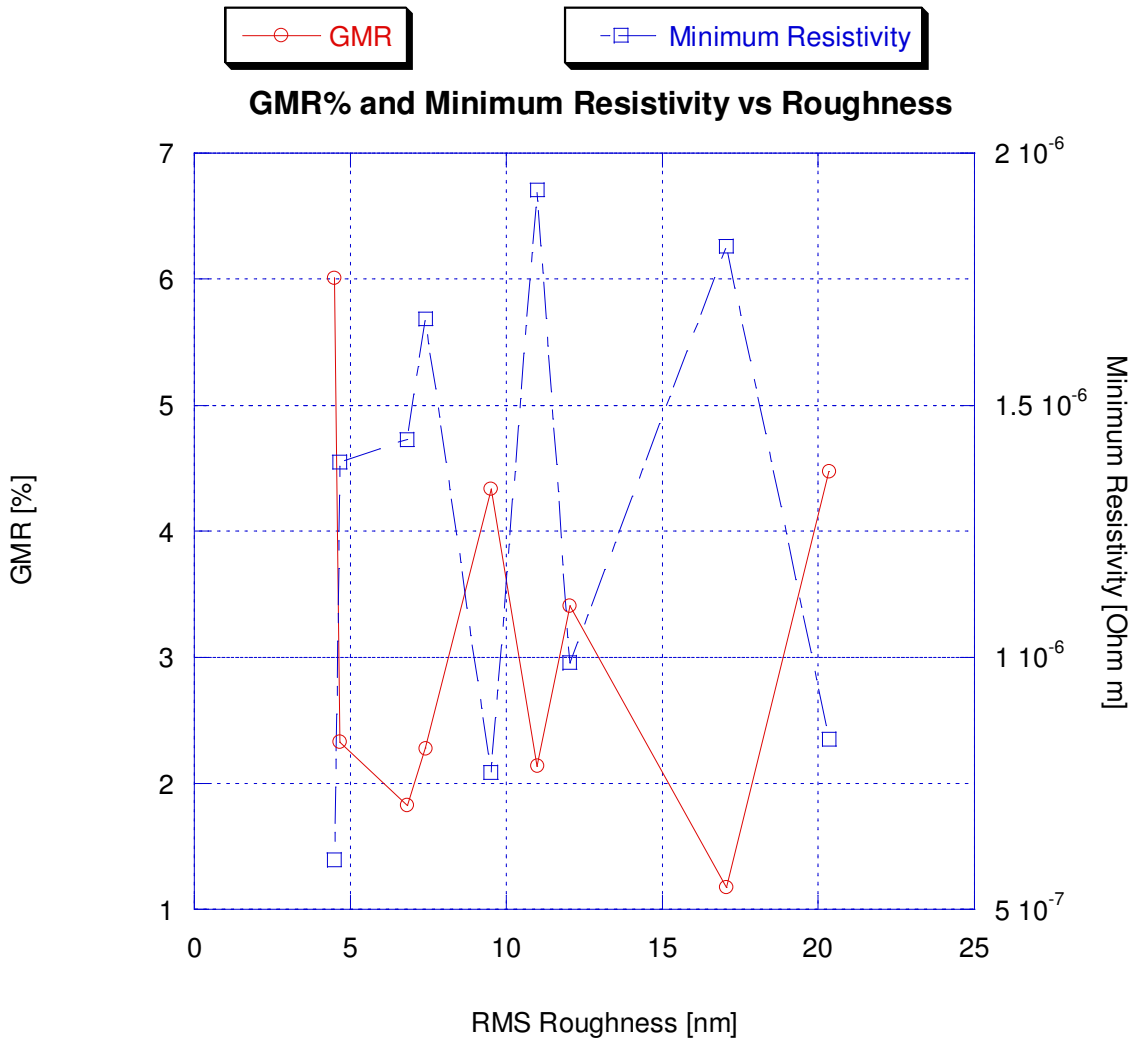

Figure 30. Minimum resistivity and GMR vs roughness in EBSV samples. Error bars are omitted to declutter the plot and line are a guide to the eye.

Next let us examine the magnetic coupling between the layers. We do not expect any major contribution of the coupling to the GMR as the data above shows. Strong coupling fields could lower GMR but obviously at the current scales this is a minor effect, requiring a higher precision experiment.

Exploring the relationship between the roughness and coupling is intriguing in itself and could provide predictions in cases when its effects on GMR are not negligible. Let us

model the coupling field using the orange peel theory alone first. This is not unreasonable since the thickness of the spacer layer varies very little if at all with the roughness. Any variation in that thickness would be the result of sputtering Cu on a rough surface. Figure 31 shows two curve fits to the data. Surprisingly the curve that assumes constant vertical roughness is a better fit. There are two possible explanations for that. The first one is that the error in the RMS roughness is so high that using it to model coupling is not possible. The second possibility is that neglecting the RKKY contribution to the coupling is not appropriate. Before we explore the second option let us see if the fit parameters make sense. Saturation magnetization M_p for the pinned Co layer is roughly going to be the saturation magnetization for bulk Co which is 18000 Gauss. The thickness of the free layer t_f is 4nm. Examining the *m2* parameter in the smooth curve fit in Figure 31 suggests that the observed wavelength is .3127±.0343 times the nanosphere size. From pure geometrical consideration in an ideal nanodot pattern we would expect that value to be ½ and this does not seem unreasonable. With this in mind and using equation (4) again we obtain that the average vertical RMS roughness is 0.135±.010nm. This seems low and suggests that we either need the residual RKKY and potentially pinhole coupling contributions included or that the roughness is lower than the measurements suggest. Although precautions were taken to prevent that from happening, measurements can be

affected from dust on the surface and impurities introduced through sputtering.

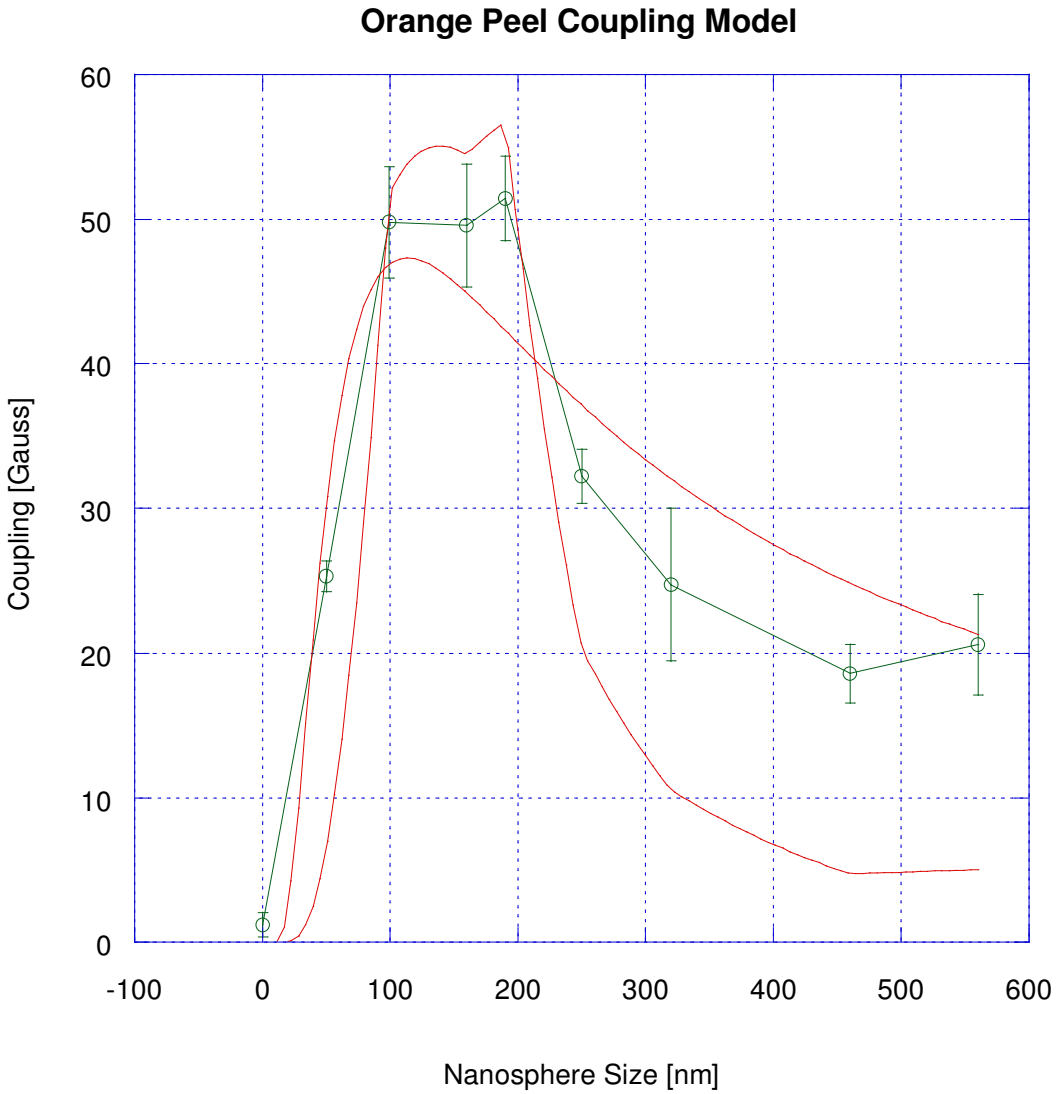

y = m1/M0*exp(-m2/M0)		
	Value	Error
m1	14628	1547
m2	113.67	12.437
Chisq	254.7	NA
R	0.94389	NA

y = h^ 2*m1/M0*exp(-m2/M0)		
	Value	Error
m1	8.5649	3.6128
m2	141.13	57.954
Chisq	1188.9	NA
R	0.70064	NA

Figure 31. Orange peel modeling of the coupling. The smooth curve assumes constant vertical roughness (as a fit parameter) and is represented be the table on the left. The piecewise smooth curve takes into account measured vertical roughness and is described by the table on the right.

The piecewise smooth fit in the table on the right of Figure 31 is not analyzed as it fits the data poorly. While the plot in Figure 32 suggests that there might be an oscillatory relationship between the vertical RMS roughness and the coupling, one look at the uncertainties tells us that it would be difficult to obtain a curve fit with any confidence. It actually proved very difficult to obtain a fit with the RKKY theory added. Even when a fit was obtained it was much worse then the one for orange peel effect alone. This is in agreement with theory and RKKY effects are indeed not substantial when roughness is introduced [16]. One last improvement to Figure 31 can be made. Introducing an offset to the curve fit improves it. This offset is in a sense an average RKKY, pinhole coupling for all the samples. Figure 33 shows this curve fit. If the offset is indeed negative as the parameter *m3* suggests then it must be predominately the result of anti-ferromagnetic RKKY coupling. The error in *m3* is large so the only thing that we can conclude with certainty is that there is no significant, if any, pinhole coupling. This curve fit gives us a wavelength to nanosphere size ratio of 0.311±.031 and an average RMS roughness of 0.142±.014. The slight increase in roughness is encouraging as the offset factor can now account for what appears to be a weak anti-ferromagnetic coupling which allows a higher orange peel coupling resulting from higher roughness.

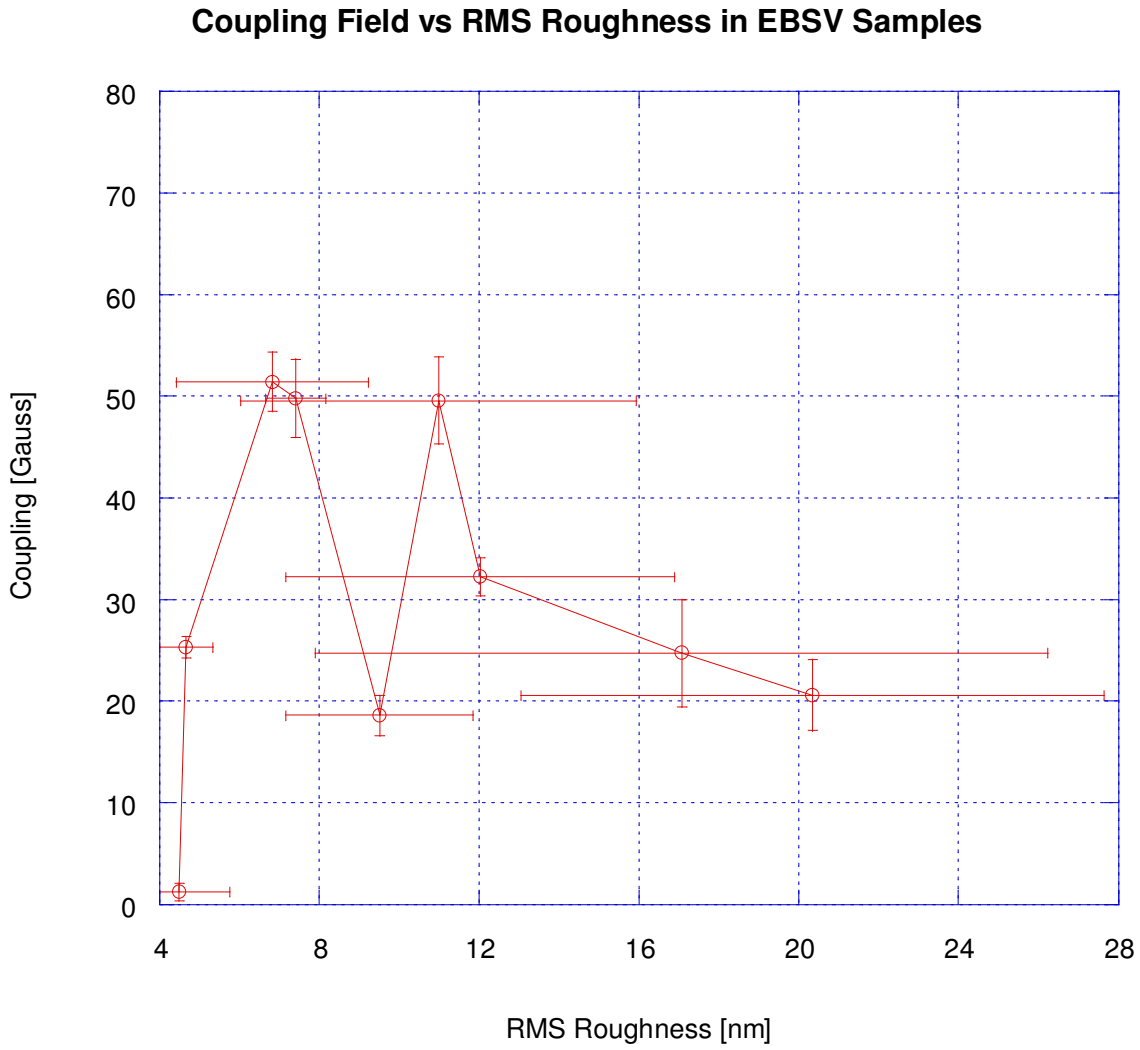

Figure 32. Coupling field in the EBSV samples versus RMS roughness. The error bars are too large to obtain a meaningful curve fit. Lines are a guide to the eye.

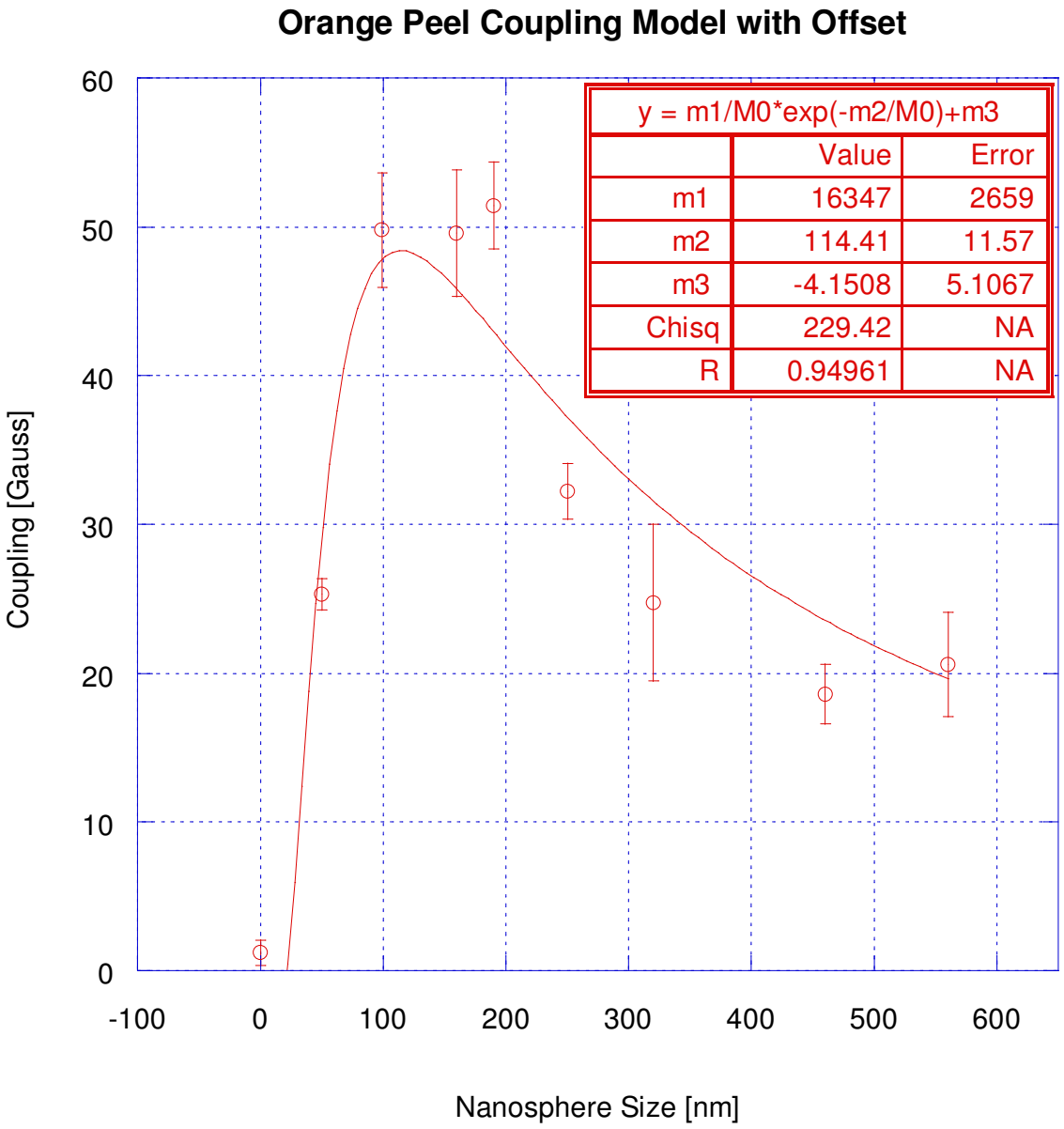

Figure 33. Orange peel fit to the coupling field with an offset.

5 Conclusions and Future Work

We have produced a series of Co/Cu EBSV and multilayers on a variety of rough substrate surfaces. Data for both Co/Cu stacks and EBSV suggests that the entire decrease in GMR% is the result of increasing resistivity. Unfortunately if there is a corresponding increase in interfacial, spin dependent scattering it is beyond the precision of the current experiment.

Producing a uniform controlled roughness proved more difficult then anticipated. As a result it is difficult to make direct models of the relationships between sample resistivity and vertical roughness. The case was similar for coupling field and vertical roughness. It is however reasonable to expect that roughness will increase the resistivity and decrease GMR in the samples.

While the coupling fields had small if any effects on GMR better understanding their behavior in rough samples is also of significant importance. In an EBSV significant ferromagnetic coupling can occur between the layers before GMR is affected. This is a direct consequence of the about 200 Gauss exchange bias and layer coercivities of about 30-60 Gauss. In Co/Cu multilayer we observed a small decrease in $\Delta\rho$ which is to be expected as a consequence of the decrease in RKKY and increase in orange peel couplings. The anti-parallel state is not fully achieved and GMR suffers. In general it appears that EBSV are more robust and would work better on novel, rough, substrates then Co/Cu stacks.

Orange peel effect seemed to account well for the coupling measured in EBSV samples. It suggested a very reasonable value for the wavelength to nanosphere size ratio

and a somewhat low value for the average RMS vertical roughness. As the desired nanodot pattern was not achieved we can only conclude that while the roughness may be periodic in nature it is very non-uniform in height and when averaged out over the entire sample not as large as anticipated. Since we only measure a cross section of about $3\mu m^2$ this is possible.

In the end the experiment would have been much more successful with the nanodot structure but even in this form the data suggests some interesting conclusions. In the future it would be great to be able to study the effects of roughness on coupling and sample resistivity with more precision in order to be able to model them and through them to model GMR. One conclusion that will likely remain the same is that the dominant effect of interfacial roughness is an increase in overall resistivity which leads to a decrease in GMR and that the orange peel effect is the major contribution to magnetic coupling between the ferromagnetic layers.

Bibliography

[1] IBM Research, "The Giant Magnetoresistive Head: A giant leap for IBM Research", http://www.research.ibm.com/research/gmr.html

[2] J. Robert Lineback, "Motorola reaches 4-Mbit milestone in development of nanocrystal memory as flash replacement", The Semiconductor Reporter (2003) http://www.semireporter.com/public/2840.cfm

[3] "Honeywell licenses Motorola's MRAM for SOI-based radiation-hard ICs" (2003) http://www.semireporter.com/public/4704.cfm

[4] M. N. Baibich *et al.*, Phys. Rev. Lett. **61**, 2472 (1988).

[5] G Binasch *et al.,* Phys. Rev. B **39,** 2428 (1989).

[6] R. E. Camley and J. Barnas, Phys. Rev. Lett. **63,** 664 (1989).

[7] R. Q. Hood and L. M. Falicov, Phys. Rev. B **49**, 368 (1994).

[8] C-L. Lee *et al.*, J. Appl. Phys. **91**, 7113 (2002)

[9] L. Neel, Comptes. Rendus **255**, 1676 (1962).

[10] L. J. van der Pauw, Philips Res. Reports **13,** 1-9 (1958).

[11] M.N. Rudden and J. Wilson, *Elements of Solid State Physics* (Wiley, New York, 1993), Second Ed., p. 98.

[12] J.R. Hook, and H.E. Hall, *Solid State Physics*, (John Wiley and Sons, New York, 1991), Second Ed., p. 220.

[13] Nicola Spaldin, *Magnetic Materials*, (Cambridge University Press, Cambridge, 2003), p. 75-106.

[14] F. Canet *et al.*, Europhys. Lett., **52** (5), 594-600 (2000).

[15] W.H. Butler, X.-G. Zhang, and J.M. MacLaren, *Journal of Superconductivity: Incorporating Novel Magnetism*, Vol. 13, No. 2, 2000, p. 221-238.

[16] J. Kudrnovsky *et al*., J. Phys.: Condens, Matter **13**, 8539 (2001)

Acknowledgments

First of all I would like to thank my advisor Dr. Reilly for all her help with the project. She gave me many opportunities over the last few years to get a head start on my thesis and guided me through the many frustrations of experimental research.

I would like to thank graduate student Shannon Watson for all her help with the project. She did most of the spin coating, and multilayer deposition for the samples used in this thesis. Our many discussions on the project and the theory were also invaluable.

I would like to also thank Olga Trofimova at the Applied Research Center at Jefferson Lab for guiding me through the AFM measurements and all her help. Last but not least I would like to thank the committee members for taking the time to evaluate this project.

Appendix I – LabView Virtual Instruments' Snapshots

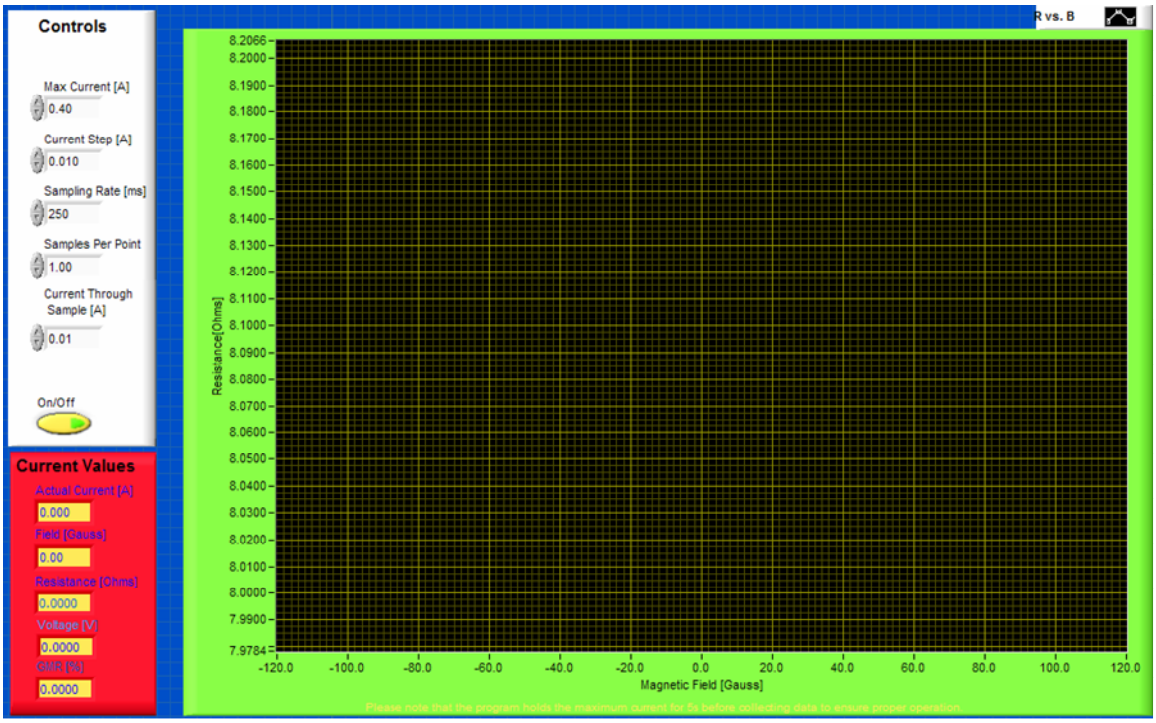

Main data collection VI. Includes three sub-programs, four step sequence structure and communicates with the power supply and voltmeter.

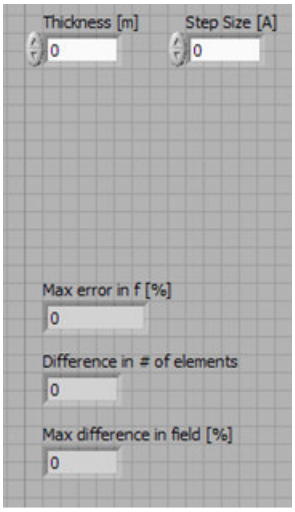

Resistivity VI. Takes two GMR plots obtained with the previous VI and outputs a single resistivity file. Based on the van der Pauw method. Includes one sub-program.